



TECHNISCHE  
UNIVERSITÄT  
WIEN  
Vienna University of Technology

## DIPLOMARBEIT

# Coherent coupling of distant $NV^-$ spin ensembles via a cavity bus

*ausgeführt am Atominstitut der Technischen Universität Wien  
unter der Anleitung von*

Univ. Prof. Dr. Hannes-Jörg Schmiedmayer

Univ. Ass. Dr. Johannes Majer

*eingereicht an der  
Technischen Universität Wien  
Fakultät für Physik  
von*

Thomas Astner

Matrikelnummer: 0828052

Schäffergasse 21/1/8, 1040 Wien

Wien, am 15. Juli 2015



*“We can only see a short distance ahead, but we can see plenty there that needs to be done.”*

Alan Turing

VIENNA UNIVERSITY OF TECHNOLOGY

# *Abstract*

Faculty of Physics

Institute for Atomic and Subatomic Physics

Master of Science

## **Coherent coupling of distant $NV^-$ spin ensembles via a cavity bus**

by Thomas ASTNER

Hybrid quantum systems - the combination of different quantum systems - serve as an ideal basis for realizing quantum information technologies. Characteristics such as long coherence times and robust control raise interest in these systems.

The thesis at hand deals with the coherent coupling of two spin ensembles spatially separated by a macroscopic distance. Electron spins of nitrogen vacancy defects in diamond are employed as spin ensemble. The coupling is mediated via a microwave coplanar waveguide resonator acting as a high quality cavity.

The device allows strong coupling of each ensemble to the cavity mode. By bringing both ensembles simultaneously in resonance with the cavity, the two ensembles behave like a single giant ensemble. The coupling strength to the cavity mode is increased by a factor  $\sqrt{2}$ , which indicates that there is a coherent energy transfer between the two ensembles and the cavity mode. This results in a spin wave, which is delocalized throughout the two spin ensembles and the cavity mode. The two ensembles are no longer distinguishable.

Furthermore, a transversal coupling between the two ensembles is proven by utilizing the dispersive cavity shift. While the spin transitions of the two ensembles are in resonance, they are far detuned from the cavity mode. The coupling between the ensembles is mediated by virtual photons. These photons do not populate the cavity. Therefore, all cavity associated loss channels can be suppressed, which allows fast probing of the system.

Additionally, the system shows excellent spin lattice relaxation times ( $T_1$ ) around 100 s at 50 mK. This is several orders of magnitude longer than the transversal spin-spin dephasing time ( $T_2$ ). Provided the  $T_2$  time scale can be extended, this architecture bears the potential for implementing a quantum memory.



# *Kurzfassung*

## **Coherent coupling of distant $NV^-$ spin ensembles via a cavity bus**

Hybride Quantensysteme - die Kombination verschiedener Quantensysteme - bilden eine ideale Grundlage für die Realisierung von Quanteninformationstechnologien. Eigenschaften wie lange Kohärenzzeiten verbunden mit stabiler und schneller Kontrolle steigern das Interesse an diesen Systemen.

In der vorliegenden Arbeit wird die kohärente Kopplung zwischen zwei räumlich getrennten Spin-Ensembles bearbeitet. Ein Spin-Ensemble wird dabei durch die Elektronenspins von Stickstoff-Defektzentren in Diamant realisiert. Die Kopplung zwischen den Ensembles erfolgt über einen supraleitenden Mikrowellenresonator. Dieser fungiert als Bussystem um Quanteninformationen kohärent zwischen den Ensembles auszutauschen. Im Transmissionsspektrum des Resonators kann der kohärente Energietransfer zwischen den Ensembles und dem Resonator direkt beobachtet werden. Die Kopplungsstärke zur Resonatormode wird um einen Faktor  $\sqrt{2}$  größer aufgrund der doppelten Anzahl von Spins. Das System verhält sich wie ein großes Ensemble, welches stark an die quantisierte Resonatormode koppelt – eine Unterscheidung zwischen den zwei Ensembles ist nicht mehr möglich.

Darüber hinaus wird eine transversale Kopplung zwischen den räumlich getrennten Ensembles über die dispersive Frequenzverschiebung des Resonators gezeigt. Die Zustandsübergänge der Spin Ensembles befinden sich zwar in Resonanz, aber sind gegen die Resonatormode verstimmt. Die Kopplung erfolgt über virtuelle Photonen, wodurch Verluste im Zusammenhang mit dem Resonator vollkommen eliminiert werden können. Dies erlaubt das schnelle Auslesen des Systems.

Das System zeigt zudem exzellente Spin-Gitter Relaxationszeiten ( $T_1$ ) in der Größenordnung von 100 s bei Temperaturen um 50 mK. Dabei liegt die Relaxationszeit einige Größenordnungen über der Spin-Spin-Dephasierungszeit ( $T_2$ ). Sofern die Zeitskala der  $T_2$  Zeit verlängert werden kann, birgt diese Architektur großes Potential für die Verwendung als Quantenspeicher.



# Contents

<b>Abstract</b>	<b>iv</b>
<b>Kurfassung</b>	<b>v</b>
<b>Contents</b>	<b>vi</b>
<b>List of Figures</b>	<b>xi</b>
<b>List of Tables</b>	<b>xiii</b>

<b>1 Introduction</b>	<b>1</b>
<b>2 Microwave Resonators</b>	<b>3</b>
2.1 Parallel Resonant Circuit . . . . .	3
2.1.1 Quality Factor $Q$ . . . . .	5
2.2 Transmission Line Resonator . . . . .	5
2.3 Coupling of a Resonator - Coupling Coefficient . . . . .	6
2.4 Coplanar waveguide (CPW) transmission line . . . . .	7
2.4.1 CPW $\lambda$ resonator . . . . .	8
<b>3 Cavity QED</b>	<b>11</b>
3.1 Jaynes-Cummings Model: Two level system cavity coupling . . . . .	12
3.1.1 The Jaynes-Cummings Hamiltonian . . . . .	12
3.1.1.1 The free field Hamiltonian . . . . .	13
3.1.1.2 The two level system Hamiltonian . . . . .	14
3.1.1.3 The interaction Hamiltonian . . . . .	15
3.1.2 Solution of the Jaynes-Cummings model . . . . .	16
3.1.2.1 Cavity - two level system interaction . . . . .	17
3.2 Tavis-Cummings Model: N two level systems . . . . .	18
3.2.1 Holstein-Primakoff approximation . . . . .	20
3.2.2 Solution of the Tavis-Cummings Model . . . . .	21
3.2.3 Cavity transmission spectrum . . . . .	21
3.2.4 Resonant Regime . . . . .	22
3.2.4.1 Strong coupling regime . . . . .	22
3.2.4.2 Weak coupling regime . . . . .	24

3.2.5	Dispersive regime . . . . .	24
3.3	Tavis-Cummings model: 2 spin ensembles . . . . .	24
3.3.1	Eigenvalue spectrum of the coupled system . . . . .	25
3.3.1.1	Dispersive Regime . . . . .	26
3.3.1.2	Losses . . . . .	27
<b>4</b>	<b>The Nitrogen Vacancy defect center in diamond</b>	<b>29</b>
4.1	Spin physics of the $NV^-$ center . . . . .	29
4.1.1	Spin transitions: single ensemble . . . . .	32
4.1.2	Spin transitions: two ensembles . . . . .	33
<b>5</b>	<b>Experimental set-up</b>	<b>35</b>
5.1	$NV^-$ ensembles on a superconducting resonator . . . . .	35
5.2	Spectroscopic set-up . . . . .	35
5.3	Cryogenic Environment - Adiabatic Demagnetization Refrigerator . . . . .	37
<b>6</b>	<b>Results</b>	<b>41</b>
6.1	Strong coupling - two ensembles . . . . .	41
6.1.1	Two ensembles on resonator no. 270 . . . . .	41
6.1.1.1	Schematics of the set-up . . . . .	42
6.1.2	Coherent coupling - collective enhancement . . . . .	43
6.1.2.1	Measurement results . . . . .	44
6.1.2.2	Parameters of the two ensembles . . . . .	47
6.1.2.3	Simulation . . . . .	48
6.2	Dispersive regime . . . . .	49
6.2.1	Initial relaxation . . . . .	51
6.2.1.1	Measurement result . . . . .	51
6.2.2	Dispersive shift background correction . . . . .	51
6.3	Transversal coupling - J coupling . . . . .	54
6.3.1	Measurement . . . . .	54
6.3.2	Transversal coupling mechanism . . . . .	55
6.3.3	Dark states . . . . .	56
6.3.4	Effects of inhomogeneous broadening . . . . .	57
6.4	Spin lattice relaxation . . . . .	58
6.4.1	Dispersive measurement - $NV^-  0\rangle \rightarrow  \pm 1\rangle$ . . . . .	60
6.4.1.1	Stretched exponential decay . . . . .	60
6.4.1.2	Temperature dependence . . . . .	61
6.4.2	Resonant measurement - $NV^- -^{13}C$ transition . . . . .	63
6.4.2.1	Wide range two tone spectroscopy . . . . .	63
6.4.2.2	Temperature dependence . . . . .	64
<b>7</b>	<b>Conclusion and outlook</b>	<b>67</b>
<b>A</b>	<b>Input impedance calculation</b>	<b>69</b>
<b>B</b>	<b>Individual and collective ensemble parameters</b>	<b>71</b>

<b>C Lorentzian fit</b>	<b>73</b>
-------------------------	-----------

<b>Bibliography</b>	<b>75</b>
---------------------	-----------

<b>Acknowledgements</b>	<b>75</b>
-------------------------	-----------



# List of Figures

1.1	The device under test . . . . .	2
2.1	RLC resonator circuit . . . . .	3
2.2	Inductance and reactance . . . . .	4
2.3	Transmission line segment . . . . .	6
2.4	CPW transmission line . . . . .	8
2.5	CPW resonator . . . . .	9
3.1	Tavis-Cummings model illustration . . . . .	11
3.2	Jaynes-Cummings illustration . . . . .	12
3.3	Jaynes-Cummings ladder . . . . .	19
3.4	Typical cavity transmission spectrum . . . . .	23
4.1	NV defect center in diamond . . . . .	30
4.2	Two ensemble illustration . . . . .	33
4.3	Two ensemble transition energies . . . . .	34
5.1	Schematics of the set-up . . . . .	36
5.2	Cryogenic setup . . . . .	37
5.3	Helmholtz coil set-up . . . . .	38
6.1	Resonator no. 270 . . . . .	42
6.2	Resonator with ensembles illustration . . . . .	43
6.3	Resonant coupling scheme . . . . .	44
6.4	Two ensemble transition energies . . . . .	45
6.5	Resonant hybridization . . . . .	46
6.6	Resonant ensemble cavity coupling . . . . .	47
6.7	Resonant ensemble cavity coupling slices . . . . .	48
6.8	Detuned ensemble cavity . . . . .	49
6.9	Dispersive measurement set-up . . . . .	50
6.10	Cavity relaxation . . . . .	52
6.11	Dispersive cavity shift . . . . .	52
6.12	Background correction . . . . .	53
6.13	Dispersive Spectroscopy . . . . .	55
6.14	Dispersive coupling scheme . . . . .	57
6.15	$NV^-$ -level spectroscopy via dispersive shift . . . . .	59
6.16	Temperature curve T1: bare $NV^-$ transition . . . . .	62
6.17	T1 statistics . . . . .	62
6.18	ADR temperature vs. time . . . . .	63

---

6.19	Wide range dispersive level spectroscopy . . . . .	64
6.20	$NV^- - {}^{13}C$ T1 versus temperature . . . . .	65
B.1	Transmission versus field spectroscopy . . . . .	72



# List of Tables

2.1	Resonator parameter . . . . .	9
6.1	Cavity resonance . . . . .	42
6.2	Ensemble parameters . . . . .	47
6.3	T1 time statistics . . . . .	61
B.1	Cavity resonance . . . . .	71



# Chapter 1

## Introduction

The goal of hybrid quantum systems is to combine the main advantages of different physical systems in order to explore new phenomena of quantum mechanics. These artificially created atom like systems bare a huge potential for future applications in quantum technology, quantum information processing and quantum metrology. The key ingredients are atoms, spins and solid state devices. They present an alliance consisting of many fields of physics such as quantum optics, condensed matter physics, atomic physics and nanosciences [XAYN13].

In 2004 Blais et. al. [BHW<sup>+</sup>04] proposed an architecture based on transmission line resonators and artificial atom-like circuits to reach the strong coupling regime of cavity quantum electrodynamics. This idea was further developed by Rabl et. al. [RDD<sup>+</sup>06], who showed how such a resonator can act as high fidelity quantum bus to mediate interaction between (ensemble) qubits. Moreover, they showed that strong coupling between such a cavity bus and a qubit allows a coherent quantum state transfer between the two systems.

### The hybrid quantum device

The electron spin of the negatively charged nitrogen vacancy color center in diamond ( $NV^-$ ) can interact via magnetic dipole interaction with the oscillating magnetic field in a cavity. In [VZK<sup>+</sup>09], [Ima09] and [WAB<sup>+</sup>09] they show that the coupling strength can be enhance by a factor  $\sqrt{N}$  (with N being the number of spins/atoms) with an ensemble of spins. This feature allows entering the strong coupling regime even if the magnetic dipole coupling of a single spin is weak. This has been shown experimentally by Amsuess et al. [AKN<sup>+</sup>11] in 2011 and Kubo et. al in 2010 [KOB<sup>+</sup>10].

The thesis at hand addresses a hybrid quantum system based on a coplanar waveguide transmission line resonator acting as quantum bus. Two ensembles of negatively charged

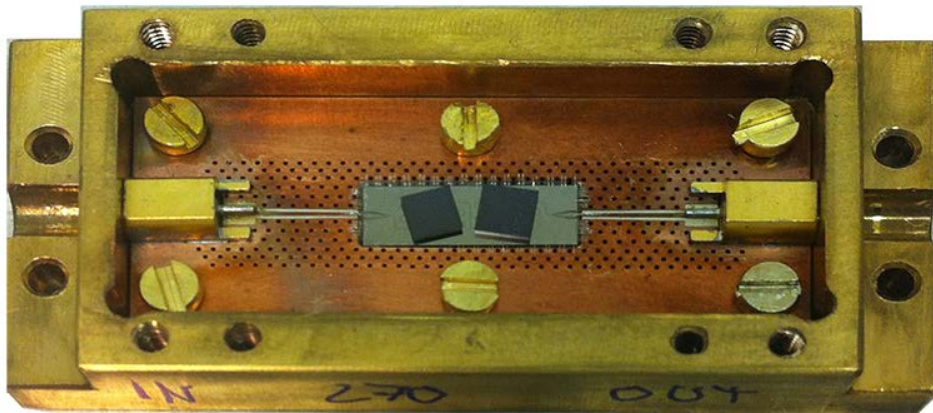


**Figure 1.1:** The hybrid quantum device under test. In the center the superconducting resonator is visible (grey rectangle). Aluminium wedge bonds connect the ground plane of the resonator with the surrounding PCB (copper). Two diamond samples containing the spin ensemble are placed on top of the resonator (black cubes).

nitrogen vacancy ( $NV^-$ ) color centers in diamond are strongly coupled to the single cavity mode. The coherent energy transfer between the two ensembles and the cavity is shown in the cavity transmission spectrum. Compared to a single ensemble the coupling strength is enhanced by a factor  $\sqrt{2}$ .

Another aspect is the investigation of a transversal coupling between the two ensembles when they are far detuned from the cavity mode.

The quantum system, which is described in this thesis can be seen in fig. 1.1. It shows the experimental realization of two ensembles on a quantum bus.

## Chapter 2

# Microwave Resonators

### 2.1 Parallel Resonant Circuit

The superconducting resonator used in this thesis is a key element for the discussed quantum device. It can be modeled as a parallel resonant circuit. In this section the basic concept behind resonant circuits shall be discussed briefly.

Resonance has an effect on the oscillation amplitude of electrical/mechanical systems, when a periodic stimulus at or close to the eigenfrequency (natural undamped frequency) of the system is applied. The oscillation amplitude for this stimulus frequency reaches a relative maximum [Gha09]. The system is able to store the excitation energy in different modes and transfers the energy between them. Therefore, the amplitude increases. The energy in the system would permanently increase without the presence of losses, leading to a resonance disaster [Kat04]. In the transfer from one energy storage mode to another, a certain amount of the energy is dissipated and consequently lost for the system (dampening). The focus shall be laid on an electric parallel resonant circuit of the RLC type (fig. 2.1). Resistor, inductor and capacitor are connected in parallel.

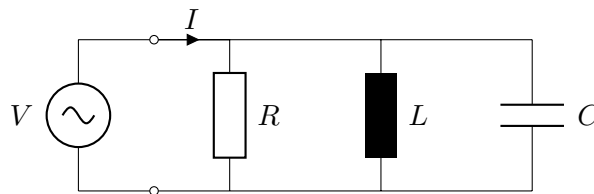


**Figure 2.1:** Lumped element RLC resonator - Schematics of an lumped element parallel RLC resonator with stimulus  $V$ .

The two modes of energy storage in this system consist of an inductor (energy of the magnetic field) and a capacitor (energy of the electric field). Assuming ideal inductor and

capacitor (no energy dissipation), the system's loss channel consists only of the resistor. Furthermore, conductance ( $G$ ), inductive ( $B_L$ ) and capacitive ( $B_C$ ) admittance can be defined for this circuit. The input impedance is subsequently given by

$$G = \frac{1}{R}, \quad B_L = \frac{1}{\omega L}, \quad B_C = \omega C$$

$$Z_{in} = \frac{1}{G + B_L + B_C} = \left( \frac{1}{R} + \frac{1}{j\omega L} + j\omega C \right)^{-1}. \quad (2.1)$$

Equation (2.1) can be approximated close to the resonant frequency  $\omega_0$ ,  $\omega = \omega_0 + \Delta\omega$  by using a Taylor series expansion in the form of  $\frac{1}{1+x} \simeq 1 - x + \dots$ . The following expression for the input impedance can be obtained (for detailed calculation see Appendix A):

$$Z_{in} = \left[ \frac{1}{R} + \frac{1}{j\omega L} + j\omega C \right]^{-1} = \left[ \frac{1}{R} + \frac{1}{j(\omega_0 + \Delta\omega)L} + j(\omega_0 + \Delta\omega)C \right]^{-1}$$

$$\approx \frac{R}{1 + j2Q_0 \frac{\Delta\omega}{\omega_0}}. \quad (2.2)$$

Figure 2.2 shows that on resonance  $\omega_0 = \frac{1}{\sqrt{LC}}$ , capacitive and inductive susceptance are equal (the imaginary part of eq. (2.1) becomes 0). Under this condition the current running through capacitor and inductor are equal. Therefore, the impedance becomes real and is purely defined by the resistance  $R$ . The power ( $P_{loss}$ ) dissipated by the resistor

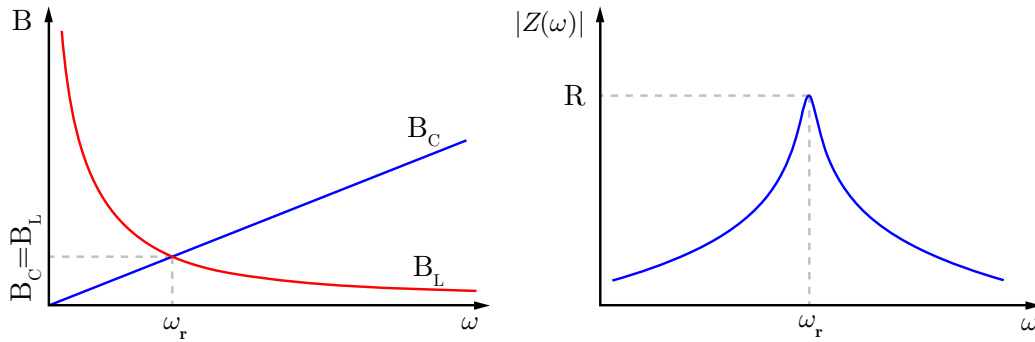


**Figure 2.2:** Graphical representation of inductive  $X_L$  and capacitive  $X_C$  reactance (left). In low (high) frequency limit the inductive (capacitive) reactance vanishes. At  $\omega_r$  both reactances are the same and the impedance is defined by the resistance. In the right figure the magnitude of the impedance is shown.

$R$  and the average storage of electrical energy ( $W_e$ ) in the capacitor and magnetic energy ( $W_m$ ) in the inductor is given by

$$P_{loss} = \frac{1}{2} \frac{|V|^2}{R} \quad W_m = \frac{1}{4} |V|^2 \frac{1}{\omega^2 L} \quad W_e = \frac{1}{4} |V|^2 C. \quad (2.3)$$

These definitions can be used to give a relation between the input power, the losses and the energy stored in the system

$$P_{in} = \frac{1}{2} Z_{in} |I|^2 = P_{loss} + 2j\omega(W_m - W_e). \quad (2.4)$$

### 2.1.1 Quality Factor Q

An important characteristic of a resonant circuit is the quality factor Q. It gives information about the power dissipation in the circuit and is defined by eq. (2.5). In the resonant case, magnetic ( $W_m$ ) and electric ( $W_e$ ) energy are equal and the internal Q factor becomes a simple expression.

$$Q_i = \omega \frac{\text{average energy stored}}{\text{energy loss/second}} = \omega \frac{W_m + W_e}{P_{loss}} = \omega_0 \frac{2W_m}{P_{loss}} = \frac{R}{\omega_0 L} = \omega_0 RC \quad (2.5)$$

High Q values indicate that the resonator is underdamped and many conversion cycles of energy, from the magnetic field energy to electric field energy, can be achieved before the oscillations decay. The frequency bandwidth in which resonance occurs is narrow for high Q resonant circuits. By coupling the resonator to an external circuit, the quality factor of the overall circuit is lowered. This is described by the so-called loaded  $Q_L$ . If a parallel resonator is loaded by an external load resistor  $R_L$ , the effective resistance is given by a parallel combination of load and resonator resistance. In [Poz11] the definition of the quality factor of the external load resistance  $\frac{R_L}{\omega_0 L}$  is shown. Hence the loaded quality factor is given by

$$\frac{1}{Q_L} = \frac{1}{Q_e} + \frac{1}{Q_i}. \quad (2.6)$$

## 2.2 Transmission Line Resonator

A segment of transmission line can be used to build a microwave resonator. The type of resonator (series or parallel) and its fundamental resonance frequency  $\omega_0$  is given by the length and termination of the transmission line element. In [Poz11] the general form of the input impedance  $Z_{in}$  of a line segment (shown in fig. 2.3) at distance  $l$  from the source as is given by

$$Z_{in} = Z_0 \frac{Z_L + Z_0 \tanh \gamma l}{Z_0 + Z_L \tanh \gamma l} \quad (2.7)$$

Depending on the termination of the line segment it can act as serial (when short circuited) or parallel (when open circuited) resonator.

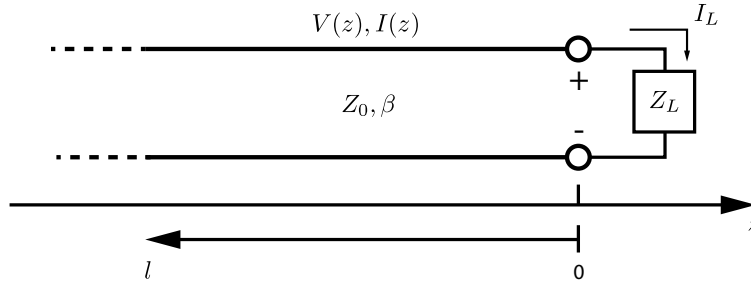


**Figure 2.3:** Transmission line segment: A piece of transmission line which is terminated with load impedance  $Z_L$

### Parallel circuit resonator

The open circuited transmission line shall be analyzed briefly. In that case the load impedance can be considered being of infinite size. Therefore, the input impedance becomes

$$Z_{in} = Z_0 \frac{1 + j \tan \beta l \tanh \alpha l}{\tanh \alpha l + j \tan \beta l}. \quad (2.8)$$

The length shall be considered to be  $l = \lambda/2$  (or any multiple). The resonance frequency is given by  $\omega_0$  and the driving frequency  $\omega$  (close to the resonance):  $\omega = \omega_0 + \Delta\omega$ . From [Poz11] the previous equation for the input impedance subsequently simplifies to

$$Z_{in} = \frac{Z_0}{\alpha l + j(\Delta\omega\pi/\omega_0)}. \quad (2.9)$$

By comparing this result with eq. (2.2), the parameters of an equivalent lumped element RLC circuit can be identified in the following way

$$R = \frac{Z_0}{\alpha l}, \quad C = \frac{\pi}{2\omega_0 Z_0}, \quad L = \frac{1}{\omega_0^2 C}. \quad (2.10)$$

The unloaded  $Q$  of the resonator can be found by using eq. (2.5):

$$Q_0 = \omega_0 RC = \frac{\pi}{2\alpha l} = \frac{\beta}{2\alpha}. \quad (2.11)$$

## 2.3 Coupling of a Resonator - Coupling Coefficient

The resonator itself is coupled to an external circuit which leads to the important quantity called coupling coefficient  $g$ . This coefficient describes the interaction of a resonator



with the external circuit to which it is connected to. From [Poz11], the coupling coefficient is given by the ratio of internal to external  $Q$ :

$$g = \frac{Q_i}{Q_e}. \quad (2.12)$$

Depending on the value of the coupling coefficient, three different regimes can be identified [FWS<sup>+</sup>05]:

- $g < 1$  Undercoupled, weak link to the external circuit, quality factor is limited by internal losses
- $g = 1$  Critical coupled, highest achievable power transfer between resonator and external circuit
- $g > 1$  Overcoupled, strong link to the external circuit, limitation of quality factor is dominated by external losses

## 2.4 Coplanar waveguide (CPW) transmission line

A coplanar waveguide is a planar type of transmission line. The conductors are in one plane, which makes manufacturing rather simple [Sim01]. Additionally, the CPW has some other advantages: isolation against crosstalk (up to 60 dB), since there are ground planes between different transmission lines. Easily accessible ground plane (no via holes/wrap-arounds necessary) which keeps the ground inductance of shunt elements low. In its simplest form a CPW transmission line consists of a center conductor, separated from ground planes by gaps. Figure 2.4 shows the basic geometry of a CPW transmission line with center conductor, ground planes and dielectric. The size of the CPW can be scaled with the ratio between  $a/b$  without changing its characteristic impedance [Sim01],[wPa]. Furthermore, a CPW transmission line supports quasi TEM-modes of the electromagnetic field. Since the dielectric constant below (substrate) and above (mostly air) the center conductor is different, a full TEM-mode support is not possible (the phase velocity in air and substrate is different). Usually the substrate is electrically thin compared to the wave length of the conveyed wave. A good approximation for the fields is the static TEM (DC, no frequency) solution [Poz11],[wPb]. With that approximation the following expressions for phase velocity  $v_{ph}$ , propagation constant  $\beta$

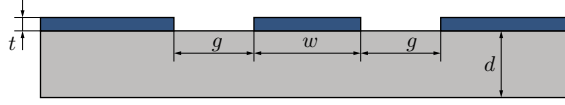


**Figure 2.4:** Schematics of a coplanar waveguide (CPW) transmission line segment on a dielectric substrate. The characteristic impedance of the transmission line is given by the dielectric constant of the substrate and the geometry relation between center conductor and gap width.

and characteristic impedance  $Z_0$  can be obtained

$$\epsilon_{eff} = \frac{C}{C_0}, \quad (2.13)$$

$$v_{ph} = \frac{c}{\epsilon_{eff}}, \quad (2.14)$$

$$\beta = k_0 \sqrt{\epsilon_{eff}}, \quad (2.15)$$

$$Z_0 = \frac{1}{C v_{ph}}. \quad (2.16)$$

With  $\epsilon_e$  denoting the dielectric constant and  $C_0$  as the line capacitance without any dielectric material present [Poz11],[CC97]. The dielectric constant of the system is geometry and material dependent. A detailed analysis to calculate the dielectric constant can be made with conformal mapping techniques for which the reader is referred to [CC97] and [Sim01]. As a rule of thumb, the resulting  $\epsilon_{eff}$  can be approximated as mean value between  $\epsilon_{substrate}$  and  $\epsilon_{air}$  [wPa].

In this work the coplanar waveguide is made out of superconducting niobium ( $T_C \approx 9.2\text{ K}$ ) thin film on a sapphire substrate.

### 2.4.1 CPW $\lambda$ resonator

The discussion of a transmission line resonator was not limited to a special type of transmission line. In nearly all experiments throughout this thesis this resonator is realized as a piece of coplanar waveguide transmission line which is coupled via coupling capacitances to a coplanar waveguide feed line. Since the focus of this work is not on the design and fabrication of these resonators, the reader is referred to the PhD thesis of Christian Koller [Kol12] who is referred to as 'master of fabrication'. In fig. 2.5 the general design of a  $\lambda$  resonator is shown. The ratio of quality factor  $Q$  and effective mode volume  $V_{eff}$  acts as a benchmark value for the quality of cavities. Compared to cavities working in the visible spectral range, coplanar waveguide microwave resonators have a typical  $\frac{Q}{V_{eff}}$  ratio in the order  $10^{13} \lambda^{-3}$ . In table 2.1 the general design parameters like resonance frequency ( $f_r$ ) and coupling capacitances ( $C_{in}, C_{out}$ ) are given.



**Figure 2.5:** Schematics of a coplanar waveguide (CPW) transmission line segment on a dielectric substrate. The characteristic impedance of the transmission line is given by the dielectric constant of the substrate and the geometry relation between center conductor and gap width. (Note: The illustration is not on scale, gap and center conductor width has been adjusted for illustration purpose).

	Resonator No. 270
$f_{res}$	2.913 GHz
$l$	43.083 mm
$C_{in}$	0.72 fF
$C_{out}$	5.7 fF
chip size	12 mm $\times$ 4 mm
$g$	8.3 $\mu$ m
$w$	20 $\mu$ m

**Table 2.1:** Design parameters of resonator no. 270.



## Chapter 3

# Cavity QED

This chapter gives a brief overview of the theoretical principles which are essential for the description of the coupling of a single spin ensemble with a single mode of electromagnetic field in a cavity. The description starts with the coupling of a single two level system to the cavity mode in the Jaynes-Cummings model. This model will be extended and adapted to describe two ensembles of  $N$  spins coupled to the cavity mode in the Tavis-Cummings model. Figure 3.1 illustrates the used Tavis-Cummings model which allows an adequate description of the investigated system.

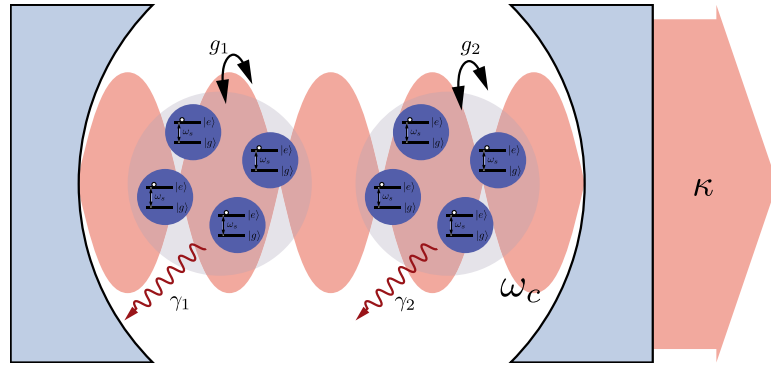


**Figure 3.1:** The figure illustrates a cavity which confines a single mode of the electromagnetic field with angular frequency  $\omega_c$ . Two ensembles of two level systems are exposed to this common radiation field in the cavity. The two level systems have a transition energy  $\omega_s$ . The coupling of the two ensembles to the cavity mode is given by  $g_1$  and  $g_2$ . Two main loss channels of the system are shown: cavity losses ( $\kappa$ ) and losses of the two ensembles ( $\gamma_1/\gamma_2$ ).

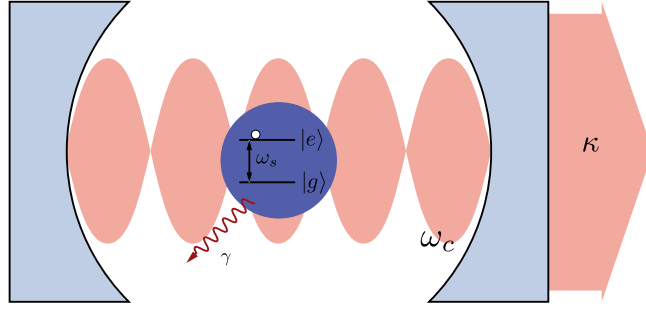


**Figure 3.2:** Illustration of the Jaynes-Cummings model: A two level system coherently interacts with a single mode of radiation in a cavity. The energy of the photons in the cavity correspond to the transition energy from the ground state to the excited state of the two level system. Losses of the cavity are given by the parameter  $\kappa$ . Two level system associated losses are given by the parameter  $\gamma$ .

### 3.1 Jaynes-Cummings Model: Two level system cavity coupling

The following section describes an atom-like system interacting with a single quantized mode of electromagnetic field in a microwave cavity. The energy of the microwave photons coincide with transition energy of the system (ground state to first excited state transition). All other energy levels are not accessible with these microwave photons and, therefore, a description of the system as an effective two-level system is applicable [Fox10]. An analysis of this problem has been first been given by Janes and Cummings [JC63], after whom this model is named, in 1963.

#### 3.1.1 The Jaynes-Cummings Hamiltonian

$$\hat{H}_{JC} = \hat{H}_{field} + \hat{H}_{spin} + \hat{H}_{int} = \hbar\omega_c a^\dagger a + \frac{1}{2}\hbar\omega_0 \sigma_z + \hbar g_0(\sigma_+ a + \sigma_- a^\dagger) \quad (3.1)$$

The first term describes the energy of the free electromagnetic field in the cavity, the second the energy of the two level system transition and the third the interaction between the two level system and the field. Figure 3.2 illustrates the basic concept of the Jaynes Cummings model Hamiltonian.

The derivation of the Hamiltonian shall be outlined and the solution briefly discussed. In [Ors07] and [Fox10] an excellent description of atoms interacting with cavities is given. All following derivations are taken from there.

### 3.1.1.1 The free field Hamiltonian

The free field Hamiltonian -  $\hat{H}_{field} = \hbar\omega a^\dagger a$  can be derived from quantizing the electromagnetic field in the cavity.

Electric ( $\mathbf{E}$ ) and magnetic ( $\mathbf{B}$ ) fields satisfy the following relations to the vector ( $\mathbf{A}$ ) and scalar ( $V$ ) potential functions,

$$\mathbf{B} = \nabla \times \mathbf{A}, \quad (3.2)$$

$$\mathbf{E} = -\frac{\partial \mathbf{A}}{\partial t} - \nabla V. \quad (3.3)$$

By making use of the Maxwell's equations in vacuum and the Coulomb gauge, a wave equation for the vector potential is obtained,

$$\nabla^2 \mathbf{A} = \frac{1}{c^2} \frac{\partial^2 \mathbf{A}}{\partial t^2}. \quad (3.4)$$

A wave solution for the vector potential and fields can be found by performing separation of variables and constructing periodic boundary conditions for allowed wave vectors  $\mathbf{k}$ . The following wave solutions for vector potential and fields are found,

$$\mathbf{A}(\mathbf{r}, t) = \sum_m \sqrt{\frac{\hbar}{2\omega_m \epsilon_0 V_{mode}}} \mathbf{e}_m \{a_m \exp[i(\mathbf{k}_m \mathbf{r} - \omega_m t)] + a_m^\dagger \exp[-i(\mathbf{k}_m \mathbf{r} - \omega_m t)]\} \quad (3.5)$$

$$\mathbf{B}(\mathbf{r}, t) = -i \sum_m \sqrt{\frac{\mu_0 \hbar \omega_m}{2V_{mode}}} \mathbf{e}_m \times \mathbf{k}_m \{a_m \exp[i(\mathbf{k}_m \mathbf{r} - \omega_m t)] + a_m^\dagger \exp[-i(\mathbf{k}_m \mathbf{r} - \omega_m t)]\} \quad (3.6)$$

$$\mathbf{E}(\mathbf{r}, t) = i \sum_m \sqrt{\frac{\hbar \omega_m}{2\epsilon_0 V_{mode}}} \mathbf{e}_m \times \mathbf{k}_m \{a_m \exp[i(\mathbf{k}_m \mathbf{r} - \omega_m t)] + a_m^\dagger \exp[-i(\mathbf{k}_m \mathbf{r} - \omega_m t)]\} \quad (3.7)$$

The summation index  $m$  includes the sum over all possible modes and polarization directions. In the case of Coulomb gauge a transversality condition for the modes is implied by  $\mathbf{e}_m \cdot \mathbf{k}_m = 0$ , which results in two orthogonal polarization directions in the plane perpendicular to  $\mathbf{k}_m$ .

From that solutions the total energy of the multi mode radiation field is obtained by

$$\begin{aligned} H &= \frac{1}{2} \int_{V_{mode}} (\epsilon_0 \mathbf{E}^2 + \frac{1}{\mu_0} \mathbf{B}^2) dv \\ &= \sum_m \hbar \omega_m (a_m a_m^\dagger + a_m^\dagger a_m) \end{aligned} \quad (3.8)$$

It is possible to identify  $a_m$  and  $a_m^\dagger$  as annihilation and creation operators, since they obey the differential equation of a harmonic oscillator. The relation to the generalized coordinate  $q$  and generalized momentum  $p$  is given by

$$a = \frac{1}{\sqrt{2\hbar\omega}}(\omega q + ip), \quad (3.9)$$

$$a^\dagger = \frac{1}{\sqrt{2\hbar\omega}}(\omega q - ip). \quad (3.10)$$

The bosonic commutation relations for the operators are

$$\begin{aligned} [a_m, a_n^\dagger] &= \delta_{nm}, \\ [a_m, a_n] &= 0, \\ [a_m^\dagger, a_n^\dagger] &= 0. \end{aligned} \quad (3.11)$$

The summation over all modes and the zero point energy can be dropped because a single cavity mode<sup>1</sup> is used. Thus, the field part of the Janes Cummings model can be written in the following form:

$$\hat{H}_{field} = \hbar \omega_c a^\dagger a. \quad (3.12)$$

### 3.1.1.2 The two level system Hamiltonian

The limitation to two accessible energy levels implies a two dimensional basis, which can be written in the form  $|\uparrow\rangle = (1 \ 0)$  and  $|\downarrow\rangle = (0 \ 1)$  with eigenenergies  $E_\pm$ . The Hamiltonian can be written as the sum over all accessible energies

$$\hat{H}_{spin} = E_+ |\uparrow\rangle + E_- |\downarrow\rangle = \begin{bmatrix} E_+ & 0 \\ 0 & E_- \end{bmatrix}. \quad (3.13)$$

---

<sup>1</sup>The used full wave  $\lambda$  resonator in principle supports two modes but the discussion here is limited to one.



The Hamiltonian can be brought in the simple form

$$\begin{aligned}\hat{H}_{spin} &= \frac{1}{2} \begin{bmatrix} E_+ + E_- & 0 \\ 0 & E_+ + E_- \end{bmatrix} + \frac{1}{2} \begin{bmatrix} E_+ - E_- & 0 \\ 0 & E_- - E_+ \end{bmatrix} \\ &= \frac{1}{2}(E_+ + E_-)\mathbf{I} + \frac{1}{2}\Delta E\sigma_z\end{aligned}\quad (3.14)$$

with  $\mathbf{I}$  being the two dimensional identity matrix,  $\Delta E = E_+ - E_- = \hbar\omega_0$  the energy difference between the two levels and  $\sigma_z$  the third Pauli matrix. Note that the zero energy is taken to be half way between the  $|\downarrow\rangle$  and  $|\uparrow\rangle$  state, implying  $E_{\pm} = \pm\frac{\hbar\omega_s}{2}$ . By neglecting the constant term  $1/2(E_+ + E_-)$ , the two level system Hamiltonian can be written in the following form

$$\hat{H}_{spin} \approx \frac{1}{2}\hbar\omega_0\sigma_z. \quad (3.15)$$

With the Pauli matrices the raising and lowering operators for the two level system are defined,

$$\begin{aligned}\sigma_+ &= \frac{1}{2}(\sigma_x + i\sigma_y) \\ \sigma_- &= \frac{1}{2}(\sigma_x - i\sigma_y).\end{aligned}\quad (3.16)$$

### 3.1.1.3 The interaction Hamiltonian

The transition of the employed two level system is in the microwave regime, corresponding to photon wavelengths in the order of a few cm. The size of the two level system is several orders of magnitude smaller than the wavelength. This condition allows one to write the Hamiltonian in the dipole approximation:

$$H_{int} = -\mu_s \mathbf{B}(\mathbf{r}, t). \quad (3.17)$$

In the case of an electron spin, the magnetic dipole moment is given by

$$\mu_s = -g_e\mu_b \frac{\mathbf{S}}{\hbar} \quad (3.18)$$

with electronic gyromagnetic factor  $g_e$ , Bohr magneton  $\mu_B$  and angular momentum  $\mathbf{S}$  of the electron. The cavity only supports stationary waves, and therefore, the single mode can be written in the form

$$\mathbf{B}(z, t) = \epsilon(a + a^\dagger) \sin(kz), \quad (3.19)$$

with  $\epsilon = \sqrt{\frac{\mu_0 \hbar \omega}{2V_{mode}}}$  being the field per photon. The Hamiltonian then becomes

$$\hat{H}_{int} = \hbar g_0 (\sigma_+ + \sigma_-)(a + a^\dagger) \quad (3.20)$$

with coupling constant  $g_0 = -\frac{\epsilon M}{\hbar} \sin(kz)$  and  $M$  as the matrix elements of the magnetic dipole operator. If eq. (3.20) is expanded, the four appearing terms can be interpreted the following way:

- $a\sigma_+$ : absorption of a photon and excitation of the two level system,  $|\downarrow\rangle \rightarrow |\uparrow\rangle$
- $a^\dagger\sigma_-$ : emission of a photon, de-excitation of the two level system,  $|\uparrow\rangle \rightarrow |\downarrow\rangle$
- $a^\dagger\sigma_+$ : emission of a photon and excitation of the two level system
- $a\sigma_-$ : photon absorption and de-excitation of the two level system

The first two processes are energy conserving and vary slowly in time. In the case of  $g_0 \ll \omega_0$ , the latter two processes do not conserve energy and vary fast in time. By applying the rotating wave approximation, all rapidly oscillating parts of the system are neglected. Then the interaction part of the Jaynes-Cummings Hamiltonian in the dipole and rotating wave approximation has the following form:

$$\hat{H}_{int} = \hbar g_0 (a\sigma_+ + \sigma_-a^\dagger). \quad (3.21)$$

### 3.1.2 Solution of the Jaynes-Cummings model

A state of the complete system is described by number states of photons in the mode and by the state of the two level system. These states have the form  $|\uparrow, n\rangle$  and  $|\downarrow, n+1\rangle$ , which are eigenstates of  $\hat{H}_0 = \hat{H}_{field} + \hat{H}_{spin}$ . These so-called 'bare' states of the unperturbed Hamiltonian have the following form:

$$\hat{H}_0 |\uparrow, n\rangle = \hbar \left( \frac{\omega_s}{2} + n\omega_c \right) |\uparrow, n\rangle \quad (3.22)$$

$$\hat{H}_0 |\downarrow, n+1\rangle = \hbar \left[ -\frac{\omega_s}{2} + (n+1)\omega_c \right] |\downarrow, n+1\rangle. \quad (3.23)$$

The ground state  $|0, \downarrow\rangle$  can be understood as no photon in the cavity and the two level system in the ground state. The energy is  $1/2\hbar\omega_c$ , which corresponds to the ground state energy of the vacuum field in the cavity. All excited states show a two-fold degeneracy. The first excited state can be described as either the two level system being in the excited state and no photon in the cavity mode ( $|\uparrow, 0\rangle$ ), or the two level system being in the ground state and one photon in the cavity mode ( $|\downarrow, 1\rangle$ ). The corresponding energy

of the first excited state is  $3/2\hbar\omega_c$  (see fig. 3.3). All other excited states have a similar form.

### 3.1.2.1 Cavity - two level system interaction

The interaction part of the Hamiltonian only couples the  $|\uparrow, n\rangle$  state to the  $|\downarrow, n+1\rangle$  state. In that case a subspace of the form  $\epsilon_n = \{|\uparrow, n\rangle, |\downarrow, n+1\rangle\}$  can be considered. The total Hamiltonian then becomes a sum of Hamiltonians acting on such subspaces:

$$\hat{H} = \sum_n \hat{H}_n \quad (3.24)$$

By introducing a detuning between cavity ( $\omega_c$ ) and two level system transition ( $\omega_s$ ) of the form

$$\Delta = \omega_s - \omega_c, \quad (3.25)$$

the Hamiltonian  $H_n$  can be written in the form

$$\hat{H}_n = \hbar\omega_c \left(n + \frac{1}{2}\right) \begin{bmatrix} 1 & 0 \\ 0 & 1 \end{bmatrix} + \frac{\hbar}{2} \begin{bmatrix} \Delta & 2g_0\sqrt{n+1} \\ 2g_0\sqrt{n+1} & -\Delta \end{bmatrix}. \quad (3.26)$$

Through magnetic dipole interaction the two fold degeneracy is lifted and after diagonalization, the following two eigenvalues are obtained:

$$E_{\pm} = \hbar\omega_c \left(n + \frac{1}{2}\right) \pm \frac{\hbar}{2} \sqrt{\Delta^2 + 4g_0^2(n+1)}. \quad (3.27)$$

The eigenstates of the full Hamiltonian can be written as a linear combination of the bare states and are the so-called 'dressed' states:

$$|+\rangle = \sin(\vartheta) |\downarrow, n+1\rangle + \cos(\vartheta) |\uparrow, n\rangle \quad (3.28)$$

$$|-\rangle = \cos(\vartheta) |\downarrow, n+1\rangle - \sin(\vartheta) |\uparrow, n\rangle. \quad (3.29)$$

The eigenvectors in eq. (3.28) can be parametrized with a mixing angle of the form

$$\cos(\vartheta) = \frac{2g_0\sqrt{n+1}}{\sqrt{(\sqrt{\Delta^2 + 4g_0^2(n+1)} - \Delta)^2 + 4g_0^2(n+1)}} \quad (3.30)$$

The splitting of the doublets can be defined as the energy differences between  $E_+$  and  $E_-$ . The phenomenon is referred to as avoided level crossing or normal mode splitting

with generalized Rabi frequency

$$\tilde{\Omega} = \sqrt{\Delta^2 + 4g_0^2(n+1)}, \quad (3.31)$$

which can be interpreted as the exchange rate of excitation between cavity and two level system.

Considering large detuning ( $\vartheta \rightarrow 0$ ), the coupling of the two level cavity system is suppressed and one finds the 'bare' states as eigenstates of the system.

In the resonant case  $\omega_c = \omega_s$ , eq. (3.30) reduces to  $\cos(\vartheta) = \sin(\vartheta) = 1/\sqrt{2}$  and the eigenvectors and eigenenergies become

$$|\pm\rangle = \frac{1}{\sqrt{2}}(|\downarrow, n+1\rangle \pm |\uparrow, n\rangle), \quad (3.32)$$

$$E_{\pm} = \hbar\omega_c \left(n + \frac{1}{2}\right) \pm \hbar g_0 \sqrt{n+1}. \quad (3.33)$$

The normal mode splitting in the resonant case is given by the Rabi frequency

$$\Omega = 2g_0\sqrt{n+1}. \quad (3.34)$$

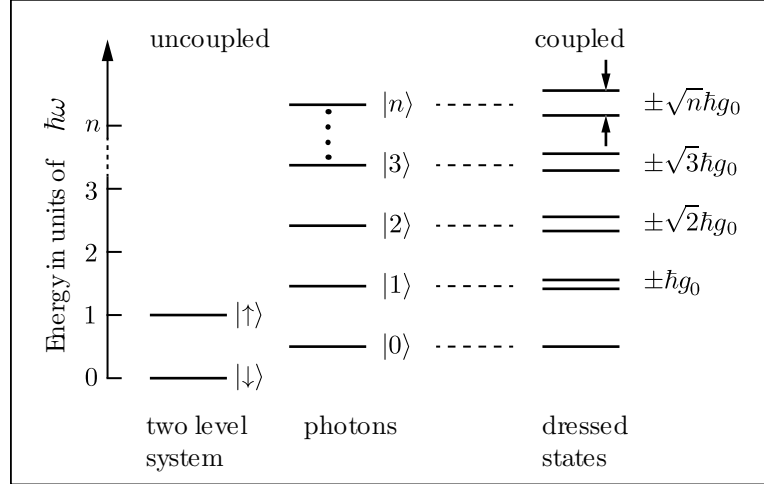
The case of  $n = 0$  is referred to as vacuum Rabi oscillation. The excited two level system emits a photon into the cavity and reabsorbs it. Therefore, the magnitude of the vacuum Rabi splitting is  $2\hbar g_0$ .

Figure 3.3 shows the Jaynes-Cummings ladder with the splitting of the two fold degeneracy of the doublets.

## 3.2 Tavis-Cummings Model: N two level systems

In 1954 Dicke showed the coherency in spontaneous radiation processes in a gas of radiating molecules. The molecules are exposed to a common radiation field. Since all molecules are interacting with the radiation field, the system should be considered as a single quantum system, rather than a system containing several independent emitters [Dic54], [TC68]. In [Gar11] details of the recent developments and mathematical description of the Dicke model can be found.

In the case described here, an ensemble of  $NV^-$  defect centers in diamond is used. They can be seen as N spins coherently interacting with a single mode of electromagnetic field in a cavity. The coupling of a single spin with the cavity mode is rather weak. Through



**Figure 3.3:** This energy ladder gives a description of a two level atom like system coupled to the radiation field of cavity photons. The uncoupled states of the two two level system are labeled with  $|\downarrow\rangle$  and  $|\uparrow\rangle$ . The uncoupled photon states are labeled by the photon numbers  $n$  in the mode.

coherent collective enhancement the coupling strength of an ensemble scales with  $\sqrt{N}$  [RTB<sup>+</sup>89], [FBB<sup>+</sup>09], [KGG<sup>+</sup>83].

To approach the description some assumptions are made:

- The spacing between the spins is large enough so that dipole-dipole interaction between the spins can be neglected.
- The radiation wavelength is in the order of cm and therefore much larger than the spin containing volume.
- Considering a large number of spins ( $10^{12}$ ), the photon number in the cavity can be set to  $n \approx 0$ .

The previously introduced Jaynes-Cummings Hamiltonian can be extended with a sum over all independent two level systems to deduce the so-called Tavis-Cummings Hamiltonian:

$$\hat{H}_{TC} = \hat{H}_F + \hat{H}_S + \hat{H}_{int} \quad (3.35)$$

$$= \hbar\omega_c a^\dagger a + \frac{\hbar\omega_s}{2} \sum_{j=1}^N \sigma_j^z + \hbar \sum_{j=1}^N g_{0,j} (\sigma_j^+ a + \sigma_j^- a^\dagger) \quad (3.36)$$

The interaction part of the Hamiltonian indicates that a single excitation in the cavity is coupled to a coherent superposition of spin excitations (spin wave) [KOB<sup>+</sup>10],

[WAB<sup>+</sup>09]. The ground state of the spin ensemble is given by

$$|\Psi_{\downarrow}\rangle = |\downarrow, \downarrow, \downarrow, \dots\rangle. \quad (3.37)$$

The first excited state is the fully symmetric Dicke state [Dic54], with a single excitation in the system:

$$|\Psi_{\uparrow}\rangle = \frac{1}{\sqrt{N}} \sum_{i=1}^N |\dots, \downarrow, \uparrow_i, \downarrow, \dots\rangle \quad (3.38)$$

As in the Jaynes-Cummings case, the interaction Hamiltonian only couples the state  $|\Psi_{\uparrow}\rangle |0\rangle$  with  $|\Psi_{\downarrow}\rangle |1\rangle$ . All other states with a single excitation in the spin system do not couple to the cavity and are referred to as subradiant.

The transition matrix element (eq. (3.39)) shows the characteristic  $\sqrt{N}$  scaling of the coupling strength<sup>2</sup>.

$$\langle 1 | \langle \psi_{\downarrow} | \hat{H}_{TC} | \Psi_{\uparrow} \rangle | 0 \rangle = \hbar \sqrt{N} g \quad (3.39)$$

It is possible to define a collective coupling strength  $g_{col}$  and eigenenergies  $E_{\pm}$  for a spin ensemble consisting of  $N$  spins as follows

$$g_{col} = g \sqrt{N} \quad (3.40)$$

$$E_{\pm} = \frac{\hbar \omega_c}{2} \pm \sqrt{\Delta^2 + 4g_{col}^2}. \quad (3.41)$$

### 3.2.1 Holstein-Primakoff approximation

Kurucz [KWM11] states that an ensemble of  $N$  spins at low temperatures (high polarization) behaves like a collection of identical harmonic oscillators. The number of spins in the ensemble is orders of magnitude larger than the number of excitations. Therefore, they consider de-localized spin waves which act as independent quasi particles. A general solution is provided by the dynamics of a single excitation. This is also valid in the case of many excitations, as long as the number of excitations is much smaller than  $N$ . Thus, the Holstein-Primakoff approximation [HP40] allows a bosonisation of the problem [KM91]. The Tavis-Cummings Hamiltonian can be written in the following form

$$\tilde{H}_{TC} = \hbar \omega_c + \hbar \omega_s b^{\dagger} b + \hbar g_{eff} (a b^{\dagger} + a^{\dagger} b) \quad (3.42)$$

---

<sup>2</sup>In that case the coupling strength is taken to be the same for every spin in the ensemble.

with  $b^\dagger = \frac{1}{g_{eff}} \sum_{j=1}^N g_j b_j^\dagger$  as the bosonic creation operator of a single excitation of the system (delocalized spin wave). The effective coupling strength  $g_{eff}$  is defined as  $g_{eff} = \sqrt{\sum_{j=1}^N |g_j|^2}$ . By assuming a homogeneous coupling strength for all spins in the ensemble ( $g_j = g$ ), the collective coupling strength is given by  $g_{eff} = \sqrt{N}g$ . This characteristic behavior of the ensemble makes it possible to reach the strong coupling regime of cavity quantum electrodynamics.

### 3.2.2 Solution of the Tavis-Cummings Model

In the discussion of this cavity two level (spin) quantum system, it was assumed that the system is fully isolated from its environment. To probe the system in the experiment it is necessary to interact with it. This is done by measuring the cavity transmission spectrum. Consequently, the system has to be treated as an open quantum system. For that, two major loss channels are introduced.

#### Cavity losses

In order to probe the cavity transmission spectrum, microwave photons have to be transmitted through the cavity. The cavity has to be designed in such a way that the photons have a certain life time in the cavity to interact with the two level system. To detect the photons from the cavity they have to be coupled out of the cavity by a semi transparent mirror. Due to this fact, cavity losses are mainly associated with mirror losses and through absorption processes. These losses are further characterized by the parameter  $\kappa$ .

#### Spin system losses

The second loss channel has its origin in the spin system itself. Not all photons which result from de-excitation of the spin system are efficiently emitted into the cavity mode and therefore are lost. All these losses, together with the spin-dephasing and spin-diffusion will be treated via the parameter  $\gamma$ .

### 3.2.3 Cavity transmission spectrum

A coherent driving field with frequency  $\omega$  and amplitude  $\eta$  is used to probe the cavity transmission spectrum. With the help of the quantum Langevin equations for the operators  $a$  and  $b$  it is possible to derive the cavity transmission as a function of the driving

field  $\omega$  in the form

$$|t(\omega)|^2 = \langle a^\dagger a \rangle = \left(\frac{\eta}{\kappa}\right)^2 \left| \frac{\kappa(i\Delta_s - \gamma/2)}{(i\Delta_s - \gamma/2)(i\Delta_c - \kappa/2) + g_{eff}^2} \right|^2. \quad (3.43)$$

$\Delta_s = (\omega - \omega_s)$  and  $\Delta_c = (\omega - \omega_c)$  as detuning of drive and cavity/spin transition. [KWM11]

Detailed analysis of the underlying problem to derive the cavity transmission can be found in [ABGP08], [CG84] and [Lax66].

If the denominator becomes zero, eq. (3.43) shows two pole type singularities. The real part corresponds to the peak position and the imaginary part contains the information of peak width of a cavity transmission spectrum with normal mode splitting (see fig. 3.4). The eigenenergies can be written in the following form with  $\Delta = \omega_c - \omega_s$ .

$$E^\pm = \hbar \frac{\omega_c + \omega_s}{2} - i\hbar \frac{\kappa + \gamma}{4} \pm \hbar \sqrt{4g_{eff}^2 - \left(\frac{\gamma - \kappa}{2} - i\Delta\right)^2} \quad (3.44)$$

From relations between the effective coupling strength and the losses, different regimes of the interaction between the spin ensemble and the cavity mode can be defined.

### 3.2.4 Resonant Regime

#### 3.2.4.1 Strong coupling regime

As shown in [KWM11], oscillating solutions for Heisenberg equations of motions in a frame rotating with the driving field are obtained, if the condition  $2g_{eff} > |\gamma/2 - \kappa/2|$  is met [HGHR98]. Strong coupling is defined as the regime where the condition  $g_{eff} \gg \kappa/2, \gamma/2$  is additionally valid. In this regime the cavity transmission shows a characteristic avoided level crossing. The two arising peaks refer to the normal mode splitting of the coupled oscillator system. The distance between the two peaks in the transmission spectrum is  $\Omega = \sqrt{4g_{eff}^2 - \frac{(\gamma/2 - \kappa/2)^2}{4}}$ . In the case of  $g_{eff} \gg (\kappa/2, \gamma/2)$ ,  $\Omega \approx 2g_{eff}$  is a valid approximation.

From the cavity transmission at the avoided level crossing the essential describing parameters of the systems can be obtained from the peak full width half maximum (FWHM) of the of the two normal modes. Figure 3.4 shows a normal mode splitting in the cavity transmission spectrum. In the experiment the FWHM of a single peak of the normal mode splitting can be seen as the average between cavity losses and spin losses:  $\Gamma = \frac{\gamma + \kappa}{2}$ . Experimentally it turned out that the cavity losses  $\kappa$  are usually one magnitude lower



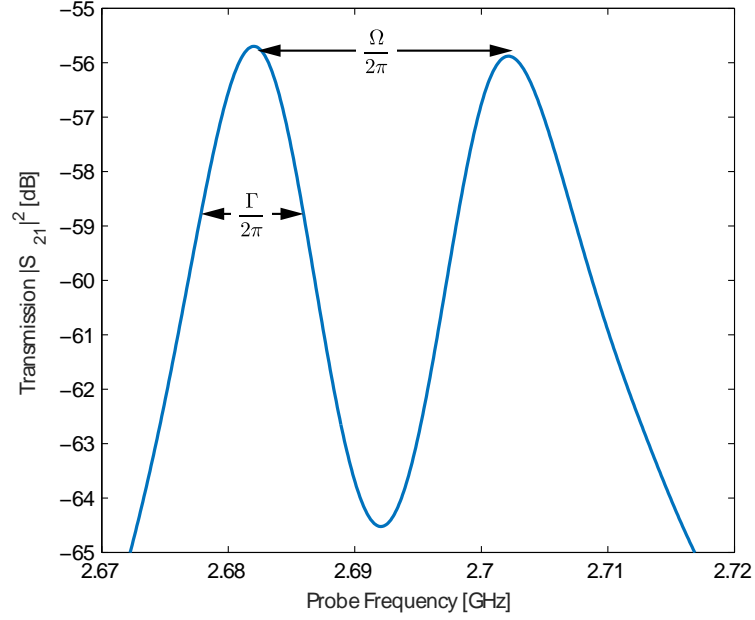


**Figure 3.4:** Transmission spectrum of the cavity spin system at resonance. The transmission shows the characteristic avoided level crossing. From the FWHM parameter  $\frac{\Gamma}{2\pi}$  of a single peak, the spin loss parameter  $\gamma$  can be determined. From the peak distance  $\frac{\Omega}{2\pi}$  the coupling strength between cavity mode and spin system can be calculated.

than the spin losses<sup>3</sup>. Hence,  $\gamma = 2\Gamma - \kappa \approx 2\Gamma$  is a valid approximation for the spin associated losses in most cases.

By setting  $\omega_c - \omega_s = 0$  in eq. (3.44) the energy (peak position) of the eigenstates can be calculated,

$$\text{Re}\left(\frac{E^\pm}{\hbar}\right) = \omega_c \pm \frac{1}{2} \sqrt{4g_{eff}^2 - \left(\frac{\gamma - \kappa}{2}\right)^2}, \quad (3.45)$$

$$\text{Im}\left(\frac{E^\pm}{\hbar}\right) = -\frac{\kappa + \gamma}{4}. \quad (3.46)$$

<sup>3</sup>The bare cavity loss parameter  $\kappa$  can be obtained from the bare cavity transmission if the spin transitions are fully saturated. This can be achieved by applying a strong drive signal. This mechanism is referred to as *bleaching* the spin ensemble. For more information see [Dru81].

### 3.2.4.2 Weak coupling regime

In this regime losses dominate over coupling strength. No normal mode splitting can be observed since  $2g_{eff} < |\frac{\gamma-\kappa}{2}|$ . This results in the following eigenvalues,

$$Re\left(\frac{E^\pm}{\hbar}\right) = \omega_c, \quad (3.47)$$

$$Im\left(\frac{E^\pm}{\hbar}\right) = -\frac{\kappa + \gamma}{4} \pm \frac{1}{2} \sqrt{\left(\frac{\gamma - \kappa}{2}\right)^2 - 4g_{eff}^2}. \quad (3.48)$$

### 3.2.5 Dispersive regime

The condition  $\Delta_{det} = |\omega_c - \omega_s| \gg (g_{eff}, \kappa/2, \gamma/2)$  refers to a regime where no energy exchange between the spin ensemble and the cavity is possible. In first order approximation, the system can be seen as uncoupled. Though spin ensemble and cavity mode are far detuned from each other, there is an interaction between them. The correction for this effect is the so-called dispersive shift given by  $\Delta_{disp} = \pm \frac{g_{eff}^2}{\Delta_{det}} < S_z >$  and arises from a series expansion of eq. (3.44) in the form  $\sqrt{1+x} \approx 1 + \frac{x}{2} - \frac{x^2}{8} + \mathcal{O}(x^3)$  for the previously obtained eigenvalues,

$$E^+/\hbar = \frac{\omega_s + \omega_c}{2} + \frac{\omega_c - \omega_s}{2} + \frac{g_{eff}^2}{\omega_c - \omega_s} - i\frac{\kappa}{2} = \omega_c + \frac{g_{eff}^2}{\omega_c - \omega_s} - i\frac{\kappa}{2}, \quad (3.49)$$

$$E^-/\hbar = \frac{\omega_s + \omega_c}{2} - \frac{\omega_c - \omega_s}{2} - \frac{g_{eff}^2}{\omega_c - \omega_s} - i\frac{\kappa}{2} = \omega_c - \frac{g_{eff}^2}{\omega_c - \omega_s} - i\frac{\kappa}{2}. \quad (3.50)$$

## 3.3 Tavis-Cummings model: 2 spin ensembles

So far, the discussion was limited to the interaction of a single ensemble containing  $N$  spins with the cavity mode. In the next step a second spin ensemble, also containing  $N$  spins, will be introduced. Thus the Tavis-Cummings Hamiltonian has to be slightly modified. An effective Hamiltonian in the following form can be defined:

$$\begin{aligned} \hat{H}_{eff} = & \hbar\omega_c a^\dagger a + \frac{1}{2}\hbar\omega_{s1}\sigma_1^z + \frac{1}{2}\hbar\omega_{s2}\sigma_2^z + \\ & + \hbar g_{eff1}(a^\dagger\sigma_1^- + a\sigma_1^+) + \hbar g_{eff2}(a^\dagger\sigma_2^- + a\sigma_2^+) \end{aligned} \quad (3.51)$$

The index  $\{1, 2\}$  refers to the two spin ensembles. Assuming a single photon in the cavity, a suitable basis for the system in that subspace is given by  $|photon, ensemble1, ensemble2\rangle$ :

$|1, \downarrow, \downarrow\rangle$ ,  $|0, \uparrow, \downarrow\rangle$  and  $|0, \downarrow, \uparrow\rangle$ . In matrix representation the Hamiltonian for this subspace has the following form:

$$\hat{H} = \hbar \begin{bmatrix} \omega_c & g_{eff1} & g_{eff2} \\ g_{eff1} & \omega_{s1} & 0 \\ g_{eff2} & 0 & \omega_{s2} \end{bmatrix}, \quad (3.52)$$

with cavity frequency  $\omega_c$ , transition energies  $\omega_{s1}/\omega_{s2}$  and coupling strengths  $g_{eff1}/g_{eff2}$  respectively. This Hamiltonian directly indicates that each ensemble couples to the cavity mode (off diagonal elements). Interesting features of this Hamiltonian can be found by looking at its eigensystem.

### 3.3.1 Eigenvalue spectrum of the coupled system

#### Resonant regime

The transition energies of the two ensembles are in resonance with the cavity and resonant with each other, hence  $\omega_c = \omega_{s1} = \omega_{s2} \equiv \omega$ . The collective coupling strength  $g_{eff1} = g_{eff2} \equiv g$  to the cavity mode is supposed to be equal for both ensembles. The Hamiltonian can be brought in the following form,

$$\hat{H} = \hbar \begin{bmatrix} \omega & g & g \\ g & \omega & 0 \\ g & 0 & \omega \end{bmatrix}. \quad (3.53)$$

The degeneracy, arising from all energies being the same, will be lifted through the coupling of each ensemble to the cavity mode. The Hamiltonian can easily be diagonalized and the following eigensystem is found with

$$E_+/\hbar = \omega + \sqrt{2}g, \quad (3.54)$$

$$E_0/\hbar = \omega, \quad (3.55)$$

$$E_-/\hbar = \omega - \sqrt{2}g, \quad (3.56)$$

as eigenenergies and

$$|+\rangle = \frac{1}{2}(-\sqrt{2}|1, \downarrow, \downarrow\rangle + |0, \uparrow, \downarrow\rangle + |0, \downarrow, \uparrow\rangle), \quad (3.57)$$

$$|0\rangle = \frac{1}{\sqrt{2}}(|1, \downarrow, \uparrow\rangle - |0, \uparrow, \downarrow\rangle + |0, \downarrow, \uparrow\rangle), \quad (3.58)$$

$$|-\rangle = \frac{1}{2}(\sqrt{2}|1, \downarrow, \downarrow\rangle + |0, \uparrow, \downarrow\rangle + |0, \downarrow, \uparrow\rangle), \quad (3.59)$$

as normed eigenvectors of the system. The  $|0\rangle$  state does not include the basis vector of a single photon in the cavity mode, and therefore, this state is experimentally referred to as dark resonance. The other two states form two normal modes (super radiant states). The two normal modes can be directly observed in the cavity transmission spectrum. An interesting aspect of this configuration is that the energy splitting between the normal modes ( $|+\rangle$  and  $|-\rangle$ ) is enhanced by a factor  $\sqrt{2}$  compared to a single ensemble in the cavity. This indicates that the system behaves like a single giant ensemble with  $2N$  spins. The excitation of the system is a superposition of a spin wave either in the first ensemble or in the second ensemble.

### 3.3.1.1 Dispersive Regime

In this regime the spin transitions of the two ensembles are in resonance with each other but far detuned from the cavity. The detuning of the two spin ensembles can be parametrized with  $\Delta = |\omega_c - \omega_{s1,s2}|$  as the detuning from the cavity frequency. As a result, the Hamiltonian has the following form,

$$\hat{H} = \hbar \begin{bmatrix} \omega & g & g \\ g & \omega + \Delta & 0 \\ g & 0 & \omega + \Delta \end{bmatrix}. \quad (3.60)$$

By further assuming  $\Delta \gg g$ , a power series expansion up to the second order correction for the eigensystem can be made. The eigenenergies become

$$E_+/\hbar = \omega_c + \Delta + \frac{2g^2}{\Delta}, \quad (3.61)$$

$$E_-/\hbar = \omega_c + \Delta, \quad (3.62)$$

$$E_0/\hbar = \omega_c - \frac{2g^2}{\Delta}, \quad (3.63)$$

with

$$|+\rangle = \frac{1}{\sqrt{2}} (|0, \uparrow, \downarrow\rangle + |0, \downarrow, \uparrow\rangle), \quad (3.64)$$

$$|-\rangle = \frac{1}{\sqrt{2}} (|0, \uparrow, \downarrow\rangle - |0, \downarrow, \uparrow\rangle), \quad (3.65)$$

$$|0\rangle = |1, \downarrow, \downarrow\rangle, \quad (3.66)$$

as normed eigenvectors of the system. From the eigensystem it is observed, that there is a coupling between the two spin ensembles even if they are far detuned from the cavity resonance frequency but in resonance with each other. Two normal modes are

formed, indicating a coherent energy transfer between the two spin ensembles. The energy splitting of the normal modes is  $\frac{2g^2}{\Delta}$ .

Within the field of classical physics an energy transfer between the two ensembles is forbidden because of the energy mismatch between cavity photons and spin transitions. However, in quantum mechanics the energy conservations can be broken for a short time (limited by the Heisenberg uncertainty relation). A photon can then be transferred from one spin ensemble to the cavity and to the other spin ensemble without populating the cavity. This virtual photon mediates the interaction between the two ensembles. Compared to an interaction with real photons, virtual photons are not lost in the cavity and it is possible to get rid of any processes of energy leaking out of the cavity. In the paper by Majer et. al [MCG<sup>+</sup>07] a similar system is shown. They couple two superconducting qubits via a cavity bus. The coupling is also mediated via virtual photons.

A detailed discussion of the transversal coupling is made in the experimental results. There also an effective Hamiltonian by eliminating all cavity parts is constructed. This alternative description reduces the problem to an interaction between two two-level systems. See section 6.3.2.

### 3.3.1.2 Losses

The previous discussion of an effective Tavis-Cummings model with two spin ensembles did not include any losses. As in the case of a single ensemble, different loss channels have to be considered. The two spin ensemble used in the experimental setup are not identical, resulting in different spin loss parameter ( $\gamma_1, \gamma_2$ ) and coupling strengths to the cavity mode ( $g_{eff1}, g_{eff2}$ ). Experimentally, these parameters are accessible if the two ensemble are separately tuned into resonance with the cavity. Accordingly, the extraction of the parameters is done in the same way as in the single ensemble case.

In the case of different coupling strengths, one has to rely on numerical methods to diagonalize the system Hamiltonian in order to derive the transition energies and eigenvalues of the coupled system.



## Chapter 4

# The Nitrogen Vacancy defect center in diamond

In the previous section the coupling of a spin ensemble to a cavity in the Tavis-Cummings model was discussed. The spin ensemble employed in this architecture is formed by a defect center in diamond. Carbon crystallizes in a face-centered cubic lattice during diamond growth. This perfect lattice can have imperfections such as lattice irregularities, substitutional atoms or interstitial impurities. In [JW06] a review about different point defects in diamond can be found. The defect discussed here is the nitrogen vacancy defect ( $NV^-$ ) color center in diamond. It consists of a nitrogen atom substituting a carbon atom and an adjacent vacancy (see fig. 4.1). The four valance electrons of carbon are covalently bond to four adjacent carbon atoms. In contrast to that, the substitutional nitrogen atom provides five electrons, which forms the neutral  $NV^0$  together with the vacancy. By capturing an additional electron from the lattice, the negatively charged  $NV^-$  is formed. It forms a trapped spin  $S = 1$  system in the diamond lattice. This spin is isolated from its environment. These unique properties and their wide spectrum of applications made the  $NV^-$  very popular in the quantum community in the last years. Long spin coherence times ( $\approx 2$  ms) even at room temperature makes this spin species an excellent candidate for quantum computing [BNT<sup>+</sup>09]. A good review paper of the NV centers capabilities as versatile sensor at nanoscale dimensions can be found in [SCLD14].

### 4.1 Spin physics of the $NV^-$ center

The  $NV^-$  possesses a paramagnetic ground state which forms a  $S = 1$  triplet. Spin-spin interactions of the two unpaired electron spins lift the degeneracy of the ground state.

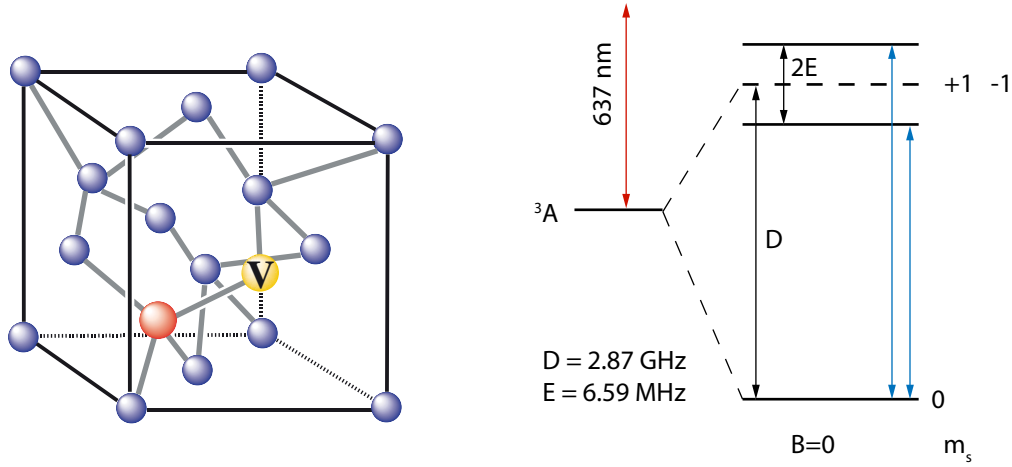


**Figure 4.1:** (left) The  $NV^-$  center as a defect in the diamond lattice. The defect is formed by an substitutional nitrogen atom and an adjacent vacancy in the lattice. (right) Simplified level structure of the  $NV^-$  center. The transition from the ground state  $m_s = 0$  to the excited spin states  $m_s = \pm 1$  is in the microwave regime.

This fine structure is the so-called zero field split (ZFS) since it is also prominent in the absence of any external magnetic or electric fields. The zero field splitting tensor is usually a rank three tensor. Due to dipolar interactions, 2 parameters are sufficient to describe the zero field splitting effects of the  $NV^-$  ground state [WJ06]. A Hamiltonian describing the ground state of the  $NV^-$  center has the following form:

$$\frac{\hat{H}_{zfs}}{h} = D(S_z^2 - \frac{1}{3}\mathbf{S}^2) + E(S_x^2 - S_y^2). \quad (4.1)$$

D and E are fine structure constants of the zero field splitting. D is a measure for the deviation of the electron wave function from spherical symmetry. The E parameter describes the deviation of the extension of the wave function in x and y directions. The effect of a local strain field is comparable to the Stark effect of an external electric field on the crystal. However, the Stark effect on the  $NV^-$  ground state is rather small. What makes the  $NV^-$  especially interesting for the coupling to a microwave cavity is the fact that its electron spin resonance (ESR) is in the microwave regime (GHz). The basic level structure of the  $NV^-$  center is shown in fig. 4.1 (left). This level scheme also includes the optical transition to an excited state. This transition allows efficient initialization of the system in the ground state (since it is not used in the thesis at hand, no detailed discussion is given here).

In contrast to the weak Stark effect, the ground state spin transitions can be efficiently tuned with the Zeeman effect. The Zeeman term in the Hamiltonian has the following



form,

$$\frac{\hat{H}_Z}{h} = -\boldsymbol{\mu} \cdot \mathbf{B}_{ext} = -g_e \beta \mathbf{S} \cdot \mathbf{B}_{ext}. \quad (4.2)$$

The factor  $g_e \beta \approx 28$  MHz/mT is a measure for the energy shift of the spin transitions.  $g_e$ , mostly called  $g$  factor, is a dimensionless number which quantifies the reaction of the magnetic moment in a magnetic field. In eq. (4.2)  $\mu$  relates magnetic moments with angular momentum and has the the following form

$$\boldsymbol{\mu} = \alpha g_e \beta \mathbf{S}, \quad (4.3)$$

where  $\alpha$  is a dimensionless number of  $\pm 1$ , indicating the sign of the charge. The Bohr magneton  $\beta$  is defined as

$$\beta = \frac{\hbar |e|}{2m_e} \quad (4.4)$$

with  $e$  as electron charge and electron mass  $m_e$ . Basis vectors for the  $NV^-$  center ground state triplet can be defined with the magnetic spin quantum number  $m_s$ , which can have the values  $m_s = 0, \pm 1$ . The resulting basis vectors are denoted as  $|0\rangle$ ,  $|1\rangle$  and  $|-1\rangle$ . In eq. (4.5) the full form of the Hamiltonian is given below in matrix form and in standard notation (see eq. (4.6)).

$$\frac{\hat{H}_{spin}}{h} = \begin{array}{c} \langle 1| \\ \langle 0| \\ \langle -1| \end{array} \begin{array}{ccc} |1\rangle & |0\rangle & |-1\rangle \\ \left( \begin{array}{ccc} D + g_e \beta B_z & g_e \beta \frac{B_x - iB_y}{\sqrt{2}} & E \\ g_e \beta \frac{B_x + iB_y}{\sqrt{2}} & 0 & g_e \beta \frac{B_x - iB_y}{\sqrt{2}} \\ E & g_e \beta \frac{B_x + iB_y}{\sqrt{2}} & D - g_e \beta B_z \end{array} \right) \end{array} \quad (4.5)$$

$$\frac{\hat{H}}{h} = D S_z^2 + E(S_x^2 - S_y^2) + g_e \beta \mathbf{B} \mathbf{S} \quad (4.6)$$

In the matrix notation (eq. (4.5)), a constant matrix  $\frac{2D}{3} \mathbf{1}$  has been added. It shifts the ground state energy to zero. In the PhD thesis of Robert Amsuess the derivation and the relations used to derive the matrix in this form can be found [Ams13]. Though the  $NV^-$  electron spin is well isolated from the environment in the diamond lattice, it can couple to other impurities present in the diamond lattice. One of the most prominent species are the two isotopes  $^{14}\text{N}$  and  $^{13}\text{C}$ . From [WRHK99] it is known that the natural occurrence of the  $^{13}\text{C}$  is approximately 1.1 %. The coupling to the nuclear spin can directly be

observed in the cavity transmission spectrum [AKN<sup>+</sup>11]. The  $^{14}N$  hyperfine interaction is omnipresent since nitrogen is a constituent of the  $NV^-$ . However, the interaction is too weak to be observed in the cavity transmission spectrum. The Hamiltonian for hyperfine interactions has the following form:

$$\hat{H}_{hf}/h = \mathbf{S}^T \cdot \bar{\mathbf{A}} \cdot \mathbf{I} \quad (4.7)$$

where  $\mathbf{I}$  denotes the nuclear spin and  $\bar{\mathbf{A}}$  as coupling tensor. From ([FEN<sup>+</sup>09] and [SCG11]) the most cited value is the  $A_{zz}$  component, which has the value  $A_{zz} \approx 130$  MHz.

### 4.1.1 Spin transitions: single ensemble

In the previous part a basis for the spin transitions was defined. From dipole transition selection rules the possible transitions are from  $|0\rangle \rightarrow |\pm 1\rangle$ . The transitions between the different spin states with and without an external magnetic field will be discussed in this part.

#### No external magnetic field

The  $|0\rangle \rightarrow |\pm 1\rangle$  transition in the absence of an external magnetic field is defined by the zero field splitting parameters  $D$  and  $E$ . The  $D$  parameter lifts the degeneracy between the  $|0\rangle$  and the  $|\pm 1\rangle$  states. Additionally the  $E$  parameter splits the  $|+1\rangle$  and  $|-1\rangle$  states by  $2E$ . Diagonalization of the spin Hamiltonian leads to the eigensystem with eigenenergies  $\epsilon = 0, D \pm E$  and respective eigenvectors  $|0\rangle = (0, 1, 0)^T$  and  $|\pm\rangle = \frac{1}{\sqrt{2}}(\pm 1, 0, 1)^T$ . The eigenstates are a linear combination of the  $|\pm 1\rangle$  states. This level mixing decreases, when an external magnetic field is applied.

#### Magnetic field in arbitrary direction

As indicated by the Hamiltonian, an external magnetic field can be used to efficiently tune the transition energies of the  $|0\rangle \rightarrow |\pm 1\rangle$  transition. Figure 4.2 (ensemble 1) shows that there are four possible neighboring lattice sites to the vacancy where the nitrogen atom can sit. If a projection of the  $NV^-$  axis is made onto the (001) plane of the crystal is made, two sub ensembles (see color code in fig. 4.2) can be identified. Depending on the angle of the magnetic field, the projection of the field amplitude on the  $NV^-$  axis is different. Hence, the two sub ensembles can be tuned collectively or independently<sup>1</sup>.

Numerical methods are used to diagonalize the Hamiltonian with an arbitrary direction of magnetic field. If the Zeeman term becomes sufficiently large,  $m_s$  becomes a

<sup>1</sup>In the experiment a 3D Helmholtz coil set-up is realized. In principle this allows also to project on any other plane than on the (001). In the experiment this degree of freedom is used to align the lab frame of reference perfectly with the (001) plane of the  $NV^-$  frame of reference.

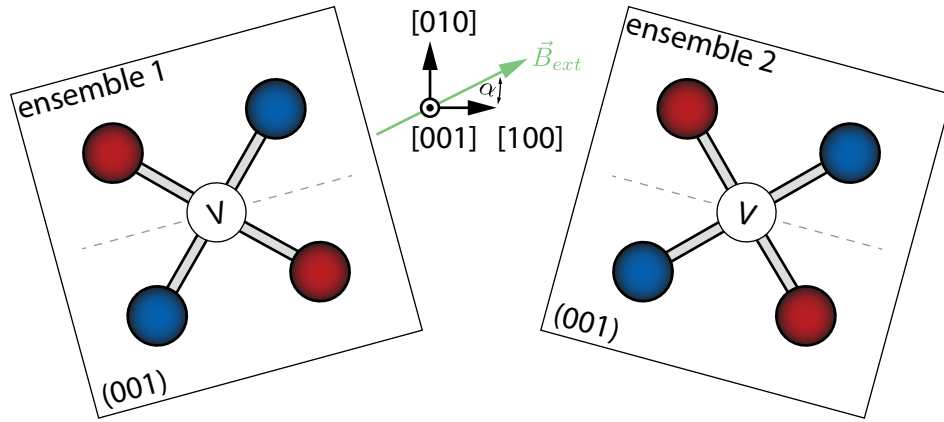


**Figure 4.2:** Two ensembles with a different twist each. The left ensemble has a twist of  $-9.1^\circ$  and the other  $15.2^\circ$ . Magnetic fields can be applied in any arbitrary direction of the (001) plane. The color code represents the two sub-ensembles that can be identified by projecting into the (001) crystal plane.

good quantum number. It is possible to determine the eigensystem and accordingly the transition energies for any arbitrary amplitude and direction of magnetic field for all possible  $NV^-$  directions. In connection with the experimental implementation, the magnetic field of the lab frame of reference has to be transformed to the crystal frame of reference.

#### 4.1.2 Spin transitions: two ensembles

If an indistinguishable second ensemble is placed into a magnetic field next to the previously discussed single ensemble, the transition energies of both ensembles are equivalent. In order to distinguish between the two ensembles and be able to tune them independently, the two ensembles are twisted relative to each other. This twist allows different magnetic field amplitudes on the resulting 4 sub ensembles. In fig. 4.2 the two separated ensembles are represented in a simplified form. The color code labels the resulting sub ensembles for each ensemble.

##### **Zeeman tuning - transition energies - $\varphi = 22^\circ$**

The first ensemble has a twist of  $\approx 15.1^\circ$  and the other ensemble of  $\approx -9.1^\circ$  (see fig. 4.2). A magnetic field is applied in the (001) plane of both crystals under an angle of  $\varphi = 22^\circ$ . In fig. 4.3 the Zeeman shift for the sub ensembles is shown. The magnetic field is applied under a constant angle ( $\varphi = 20^\circ$ ) relative so a global frame of reference.

##### **Zeeman tuning - transition energies - $\varphi = 48.1^\circ$**

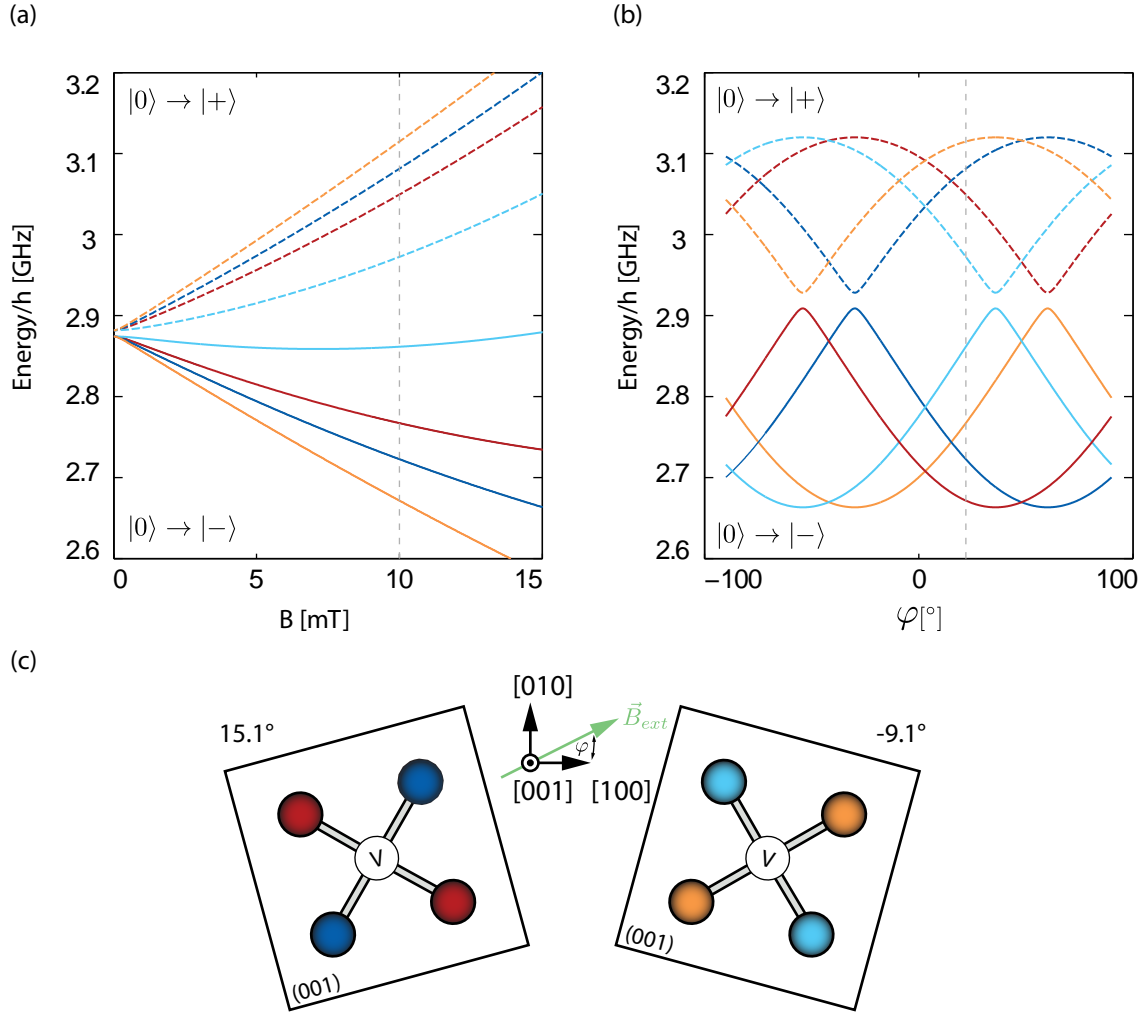


**Figure 4.3:** Spin transitions of the two  $NV^-$  ensembles. (a) Spin transition  $|0\rangle \rightarrow |- \rangle$  (solid lines) and  $|0\rangle \rightarrow |+ \rangle$  (dashed line) versus the magnetic field amplitude. The angle was kept constant at  $\varphi = 22^\circ$  (vertical line in (b)). (b) Transition energies of the two ensembles for different orientations of the magnetic field in the (001) plane. The used amplitude is indicated by the vertical line in (a). (c) Colors indicate the different sub-ensembles which arise from applying the field in the (001) plane. Colors correspond to the colors in (a) and (b).

If a magnetic field is applied under an angle of  $\varphi = 48.1^\circ$ , the projection of the field amplitude on the sub ensembles are the same for both ensembles. Hence, the transition energies for the sub ensembles is the same - the system is degenerate. Due to the different twist of the two crystals, a degree of freedom is added to the system. This allows tuning of the transition energies of the sub ensembles in the two crystals with respect to each other. With a rotation of the magnetic field the transition energies can be brought into resonance (degenerate) or out of resonance. With this degrees of freedom, a wide range of configurations for the spin transitions can be realized.

## Chapter 5

# Experimental set-up

The underlying theoretical concepts of this quantum system was outlined and discussed in the previous chapters. Here, the experimental environment and the measurement set-up shall be introduced and explained, followed by a presentation of the obtained results.

### 5.1 $NV^-$ ensembles on a superconducting resonator

With respect to the Jaynes-Cummings model, a description of a cavity quantum system has been given. This model has been extended to the Tavis-Cummings model for two spin ensembles. The spin ensemble was realized as  $NV^-$  defect centers in diamond. A superconducting  $\lambda$  resonator was presented, acting as high Q cavity. With these parts it is now possible to assemble the quantum system discussed in this work. Figure 5.1 shows the built quantum device which is used in most experiments. The copper sample box which houses the device is closed by a lid with spring loaded pogo pins, holding the two diamonds in place. The box itself establishes boundary conditions for the electromagnetic field in a way that no standing waves (box resonances) can occur in the frequency domain of interest.

### 5.2 Spectroscopic set-up

In all measurements the cavity transmission spectrum is probed with a vector network analyzer (VNA). The VNA provides phase coherent continuous wave microwave signals from 4 kHz up to 8.5 GHz. From the VNA the forward voltage gain  $S_{21}$  scattering

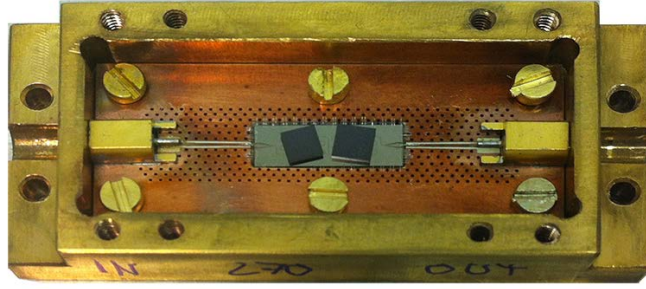


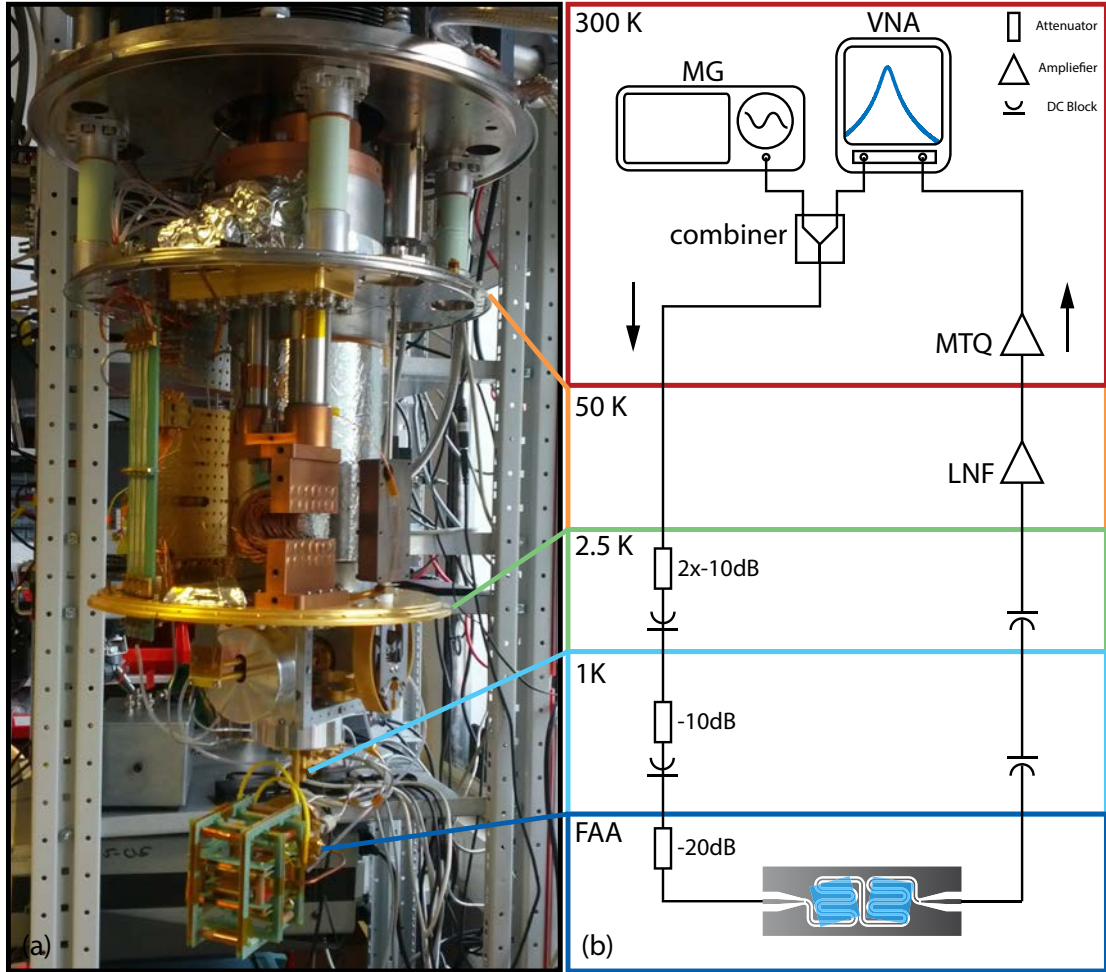
**Figure 5.1:** Experimental realization of the quantum device. Two diamonds with  $NV^-$  spin ensembles are placed on a superconducting  $\lambda$  resonator (grey part in the center). The superconducting chip is connected via aluminum bond wires to the ground plane of the surrounding PCB (copper). The PCB supports mini SNP connectors.

parameter is obtained. It is defined the ratio between the wave amplitude coming out of port 2 and the amplitude of the incident wave on port 1:  $S_{21} = V_2^-/V_1^+$  [Poz11].

The sample itself is mounted at the lowest stage of a adiabatic demagnetization cryostat (ADR). The input line, which goes down from room temperature to the sample, has several microwave attenuators and DC blocks. On the one hand, the attenuators avoid thermal noise from stages at higher temperature leaking to the sample. On the other hand, they thermally couple the inner conductor of the coaxial lines to the different thermal stages of the fridge. This avoids heating of the device.

For single photon experiments it is advisable to equip the up line after the device with microwave circulators. Unlike as in the down line, it is not possible to use attenuators because they would counteract the amplification of the microwave signal. Circulators act like a one way valve for microwaves and therefore shield the device from thermal noise entering from the up line side. In this set-up and for the experiments carried out throughout this thesis, no circulators were necessary. Another important part is the amplifier for cryogenic environment. In this set-up an amplifier from the company Low Noise Factory was used. The amplifier has a gain of +39 dB in a frequency domain of 4-8 GHz (also properly operates around 3 GHz). The typical noise temperature is in the order of 2.1 K. At room temperature an additional ultra low noise amplifier from MITEQ is used. The gain of this amplifier is +30 dB at 3 GHz with a noise temperature of 50 K. The signal is then fed to port 2 of the network analyzer.

To use the full ability of tuning transition energies for both spin ensembles, 3D Helmholtz coil pairs are mounted around the device at the lowest stage (FAA). It gives the freedom to align the magnetic field perfectly with the resonator and the diamond (001) plane. Further magnetic fields up to 15 mT in all directions can be applied. The mounted coil set-up can be seen in fig. 5.3.



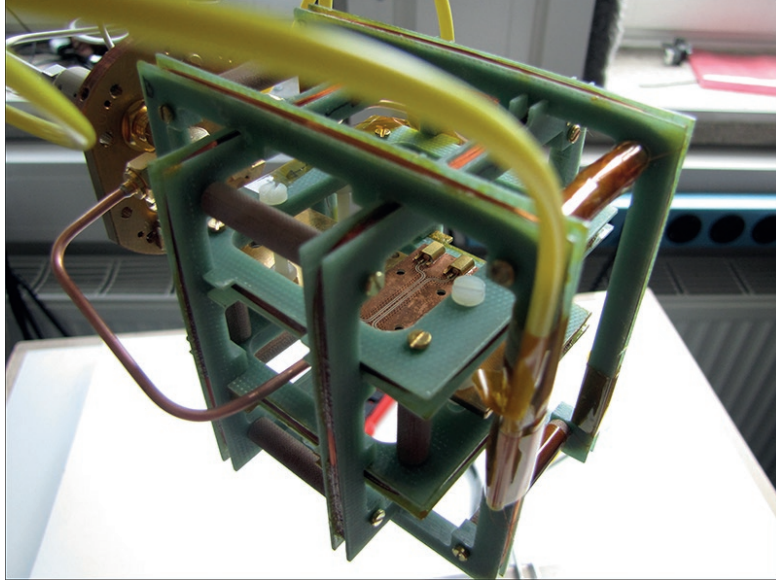
**Figure 5.2:** (a) The used fridge with its different temperature stages. (b) Schematics of the used measurement set-up with its main components. The microwave generator (MG) is not used in all experiments.

Figure 5.2 gives an overview of the used spectroscopic measurement set-up in the ADR.

### 5.3 Cryogenic Environment - Adiabatic Demagnetization Refrigerator

In order to provide a high polarization of the spin system in the ground state and keep thermal excitations low, a cryogenic environment is needed. For the experiment discussed here an adiabatic demagnetization refrigerator (ADR) is used to carry out measurements below 100 mK. The ADR is based on the magnetocaloric effect (MCE), first discovered by E. Warburg [E.81]. Since this technology is also a promising candidate for entering conventional markets for substitution of vapor compression refrigeration [RFDR13], a brief discussion concerning the magnetocaloric effect used in a cooling





**Figure 5.3:** 3D Helmholtz coil mounted at the FAA stage of the ADR. Semi rigid copper coaxial lines are connected to a CPW transmission line.

cycle shall be given here. The MCE is the thermal response of a material when exposed to a change of external magnetic field. The effect can be either cooling or heating of the material. To understand this property of magnetic materials, one has to take a look at the total entropy of the material. Pecharsky [PGPT01] states that the entropy of a magnetic material is given by

$$S_T(H, T) = S_m(H, T) + S_l(T) + S_e(T) \quad (5.1)$$

where the total entropy ( $S_T$ ) is the sum of three individual entropies of the material:  $S_m$  (magnetic entropy of the magnetization),  $S_l$  (entropy of the lattice) and  $S_e$  (entropy of the electrons). The field dependence of lattice and electron entropy has been neglected in first order approximation. In general, all three parts have a dependence on magnetic field [TS03]. By applying a magnetic field on such a material, an adiabatic change of temperature can be induced. The spins align in the magnetic field. Therefore, magnetic entropy is reduced, electron and lattice entropy has to compensate for that decrease in entropy to maintain adiabaticity. Consequently, the temperature of the material rises. By turning off the magnetic field, the spin system is able to return to its initial configuration by draining energy from the lattice, bringing the system back to its temperature before magnetization. The process is fully reversible. To use this physical property for cooling in the mK regime, the heat which originates from applying a magnetic field has to be removed. In the ADR this is done by a pulse tube cooler.

In the next step the external magnetic field is gradually ramped down. The system has maintained its initial temperature (isothermal process). The increase in magnetic



entropy has to be compensated by the lattice and therefore the temperature is reduced.

As mentioned before, an isothermal process is needed to remove the heat that is produced while aligning the spins in the magnetic field. The used pulse tube cooler works according to the Stirling engine principle. The advantage of the pulse tube cooler is that it can be built without any moving parts and has low maintenance.

### **Experimental relevance**

The cooling capability of a cryogenic device is usually quantified with its cooling power. In the case of an ADR it is important to notice that this is not applicable. The ADR has a finite cooling energy because of the used principle. With installed equipment (coils, microwave cabling, sample stage) the energy is sufficient to reach a base temperature around 50 mK. The temperature then gradually starts to rise. After a full demagnetization of the magnetic material, another cycle of magnetization followed by demagnetization must be carried out. Instead of a full demagnetization, the ADR offers the possibility to dose the applied cooling energy. This is usually done by linearly ramping down the magnetic field of the fridge and, therefore, continuously spending the energy to maintain a certain temperature. The fridge can remain at 70 mK for approximately 12 hours, which is a sufficient amount of time for the experiments carried out in the thesis at hand.

### **Necessity of a cryogenic environment**

To enter the quantum mechanical regime of an integrated circuit, all dissipation losses have to be eliminated. This can be achieved by using low temperature superconducting materials such as niobium ( $T_C \approx 9.25 \text{ K}$ ) or aluminum ( $T_C \approx 1.2 \text{ K}$ ) [DWM04]. This guarantees that no energy is lost, hence quantum coherence can be maintained.

Furthermore it is important to embed the quantum system in a low thermal noise environment. Temperatures at which the energy of thermal fluctuations ( $k_B T$ ) are much smaller than the transition energy  $\hbar\omega_{\downarrow \rightarrow \uparrow}$  of the two level system have to be reached. Since the spin transitions are in the regime of 2 - 3 GHz, a temperature below 100 mK is indispensable (2 GHz corresponds to approximately 95 mK) [DWM04]. At these temperatures the polarization of the spin system in its ground state is high enough to carry out experiments.



# Chapter 6

## Results

The aim of this chapter is to present the obtained measurement data in combination with calculations based on the theoretical concepts derived previously. The first measurement series concerns the coupling of the two spin ensembles to the cavity mode. The coherent collective coupling of two spatially separated spin ensembles is shown through the characteristic  $\sqrt{2}$  scaling of the coupling strength.

In the second part a direct ensemble-ensemble coupling of the two macroscopically separated  $NV^-$  ensembles is shown. This coupling is achieved via virtual photons, which do not populate the cavity.

The final part deals with determination of the spin lattice relaxation time (T1) of a single  $NV^-$  ensemble and with a  $NV^- -^{13}C$  ensemble. Both types show very long T1 times which demonstrate the performance of these spin-cavity systems for applications in quantum information technology.

### 6.1 Strong coupling - two ensembles

#### 6.1.1 Two ensembles on resonator no. 270

Figure 6.2 shows an illustration of the presented device. The generally used  $\lambda/2$  resonator design was modified, from which the design of a full wave  $\lambda$  transmission line resonator derived. The design suggests resonance peaks at 1.4 GHz and 2.8 GHz. The unloaded frequency is slightly above the  $|0\rangle \rightarrow |-1\rangle$  transition of the spin ensemble. After loading the resonator with the two diamond samples, the resonance shifts to lower frequencies. The change in the dielectric constant above the resonator is noticeable in the resonance frequency and quality factor. In fig. 6.1 the obtained line profile of the resonator is shown.

	(b) unloaded	(a) loaded <sup>1</sup>	$\Delta$
$\frac{\omega_c}{2\pi}$	2.910 GHz	2.747 GHz	−163 MHz
$Q$	63 200	23 500	−39 500
$\frac{\kappa}{2\pi}$	46 kHz	420 kHz	374 kHz

**Table 6.1:** Measured parameters of unloaded and diamond loaded cavity no. 270.

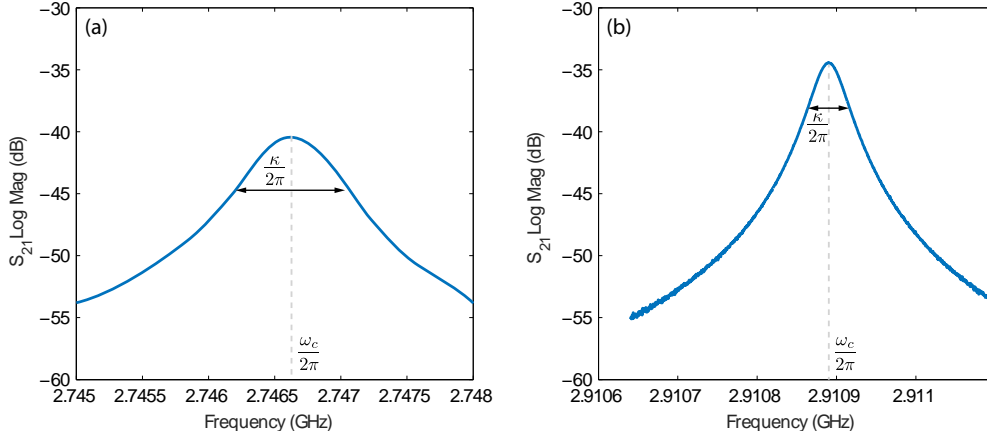


**Figure 6.1:** (a) Resonator with diamond samples on top. Parameters like amplitude, resonance frequency and quality factor decrease because of dielectric loading. (b) Trace of the empty resonator no. 270. A Lorentzian line shape has been fitted to the traces. Note: The frequency span has to be chosen different in both plots, since the full width half maximum bandwidth is different between the two traces.

To extract the parameters resonance frequency  $\omega_c$ , loss parameter  $\kappa$  and quality factor  $Q$ , a Lorentzian line shape was fitted to the measured profile. Table 6.1 summarizes the measured parameters for the unloaded and diamond loaded cavity. A brief introduction on fitting resonances and which functions are used can be found in appendix C.

### 6.1.1.1 Schematics of the set-up

Each diamond sample is placed on the resonator with a different twist (see fig. 6.2). The magnetic field (indicated as the red arrow in the illustration) allows tuning of the transition energies of both ensembles. Due to the different twist of each diamond, the projection of the magnetic field is different for each ensemble. At  $48.1^\circ$  the field amplitude is the same for both ensembles and transitions of both ensembles can be tuned into degeneracy. For the calculations of the transition energies of the two ensembles, one

<sup>1</sup>The value was obtained at a temperature of 950 mK. The spin polarization is low enough to measure the pure cavity resonance. In section 6.4 it will be shown, that at this temperatures, the influence of the spin system is negligible.

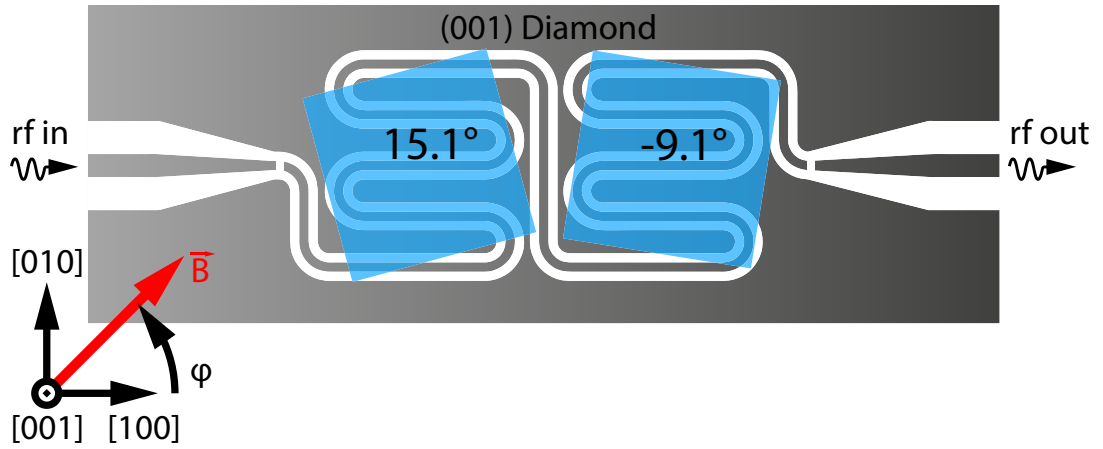


**Figure 6.2:** Superconducting resonator with two diamond samples on top. Magnetic fields are applied in the (001) plane of both crystals. The transmission through the device is probed with a VNA.

has to keep in mind that a conversion from the lab frame of reference (Helmholtz coil set up) to the individual crystal frame of reference is necessary (also see section 4.1.2).

### 6.1.2 Coherent coupling - collective enhancement

With the help of the introduced theory it is possible to calculate the eigenenergies for the two ensemble cavity system as a function of amplitude and angle of the magnetic field. In fig. 6.4 (a) the transition energy ( $|\downarrow\rangle \rightarrow |\uparrow\rangle$ ) spectrum of the two ensembles and the cavity is shown<sup>2</sup>. In plot (a) all coupling terms are neglected ( $g$  is set to zero in the Hamiltonian). The pure transition energies (green and red) and the cavity mode (blue) are degenerate at certain field angles (crossings of green, red and blue). In subplot (b) the coupling of a single ensemble to the cavity mode is taken into account. The two blue lines (cavity mode) originate from single ensemble coupling Hamiltonians. The transition energies and resonator eigenvalue are plotted in one figure. The uncoupled eigenvalues are plotted in grey. At  $48.1^\circ$  the transition energies of the two ensembles are still degenerate (red line crosses green).

In fig. 6.4 (c) the transition energies of the total system, taking into account all couplings, are plotted. The degeneracy between the two ensembles at  $48.1^\circ$  is lifted. The system shows 3 distinguishable states. By referring to the theory discussed in section 3.3.1, the three states at an field angle of  $\varphi = 48.1^\circ$  can be mapped to the following eigenstates of

<sup>2</sup>In the experiment the interesting  $NV^-$  transition is from the  $m_s = 0$  to  $m_s = -1$  state. Subsequently this transition is represented as  $|\downarrow\rangle \rightarrow |\uparrow\rangle$ .

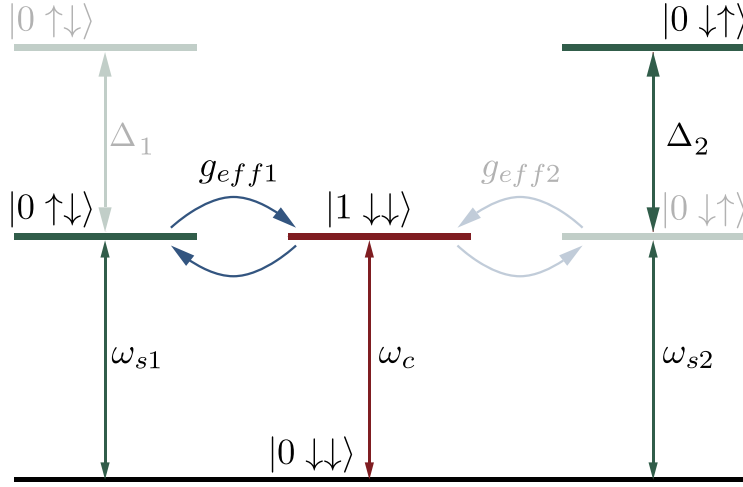


**Figure 6.3:** Resonant coupling scheme: ensemble 1 and ensemble 2 can be independently tuned in resonance with the cavity mode. Each ensemble couples with its coupling strength  $g_{eff1,2}$  to the cavity mode. By setting the detuning  $\Delta$  of each ensemble to zero, they collectively couple to the cavity mode.

the system,

$$\begin{aligned}
 |+\rangle &= \frac{1}{2}(|0 \uparrow\downarrow\rangle + |0 \downarrow\uparrow\rangle + \sqrt{2}|1 \downarrow\downarrow\rangle) \\
 |0\rangle &= \frac{1}{\sqrt{2}}(|0 \downarrow\uparrow\rangle - |0 \uparrow\downarrow\rangle) \\
 |-\rangle &= \frac{1}{2}(|0 \uparrow\downarrow\rangle + |0 \downarrow\uparrow\rangle - \sqrt{2}|1 \downarrow\downarrow\rangle).
 \end{aligned} \tag{6.1}$$

where  $|0\rangle$  belongs to the purple line at  $48.1^\circ$ .

The coupling scheme in which each ensemble couples to the cavity mode on resonance is also graphically represented in fig. 6.3. The scheme elucidates the possibility of coupling each ensemble independently to the cavity mode or both simultaneously.

### 6.1.2.1 Measurement results

Figure 6.6 (a) shows the magnitude of the  $S_{21}$  scattering parameter versus the angle of the magnetic field in the (001) crystal plane. Around  $10^\circ$  and  $90^\circ$  the dominating amplitude is given by the resonance peak of the resonator ( $\approx 2.745$  GHz). In this angle span, the spin transitions are far off resonant with the cavity. Still the  $NV^-$  spin transitions are visible in the transmission spectrum.

By rotating the magnetic field the  $|\downarrow\rangle \rightarrow |\uparrow\rangle$  transition of the first ensemble crosses the resonator at approx.  $20^\circ$ . An avoided level crossing is observed in the cavity transmission

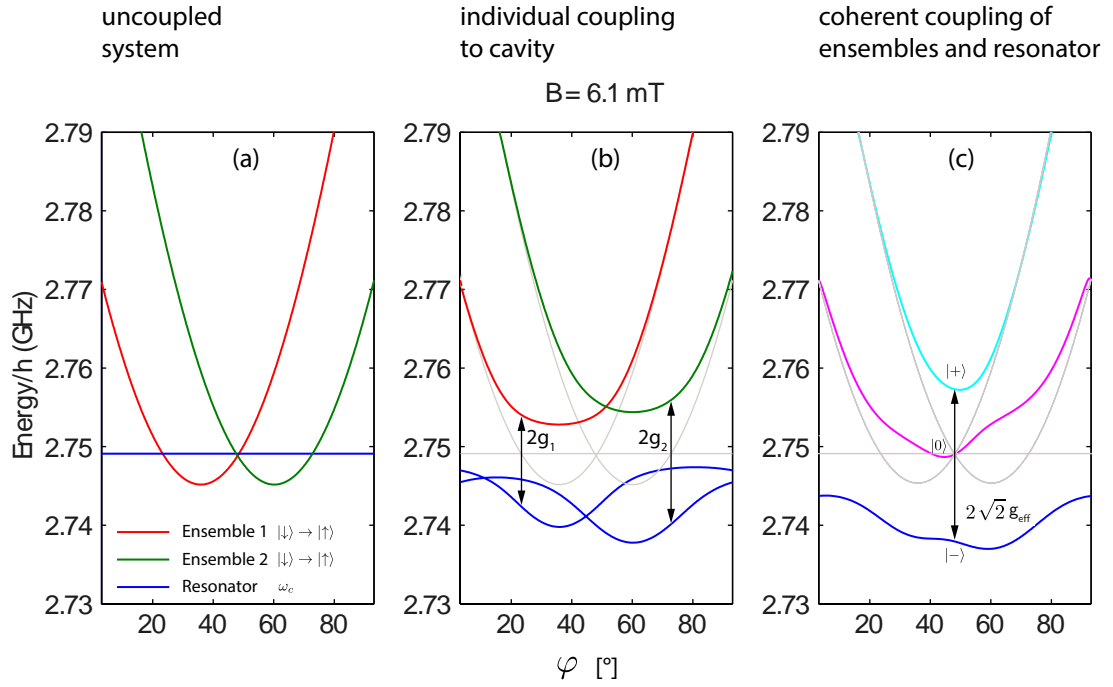


**Figure 6.4:** (a) Transition energies of the uncoupled system. (b) each ensemble couples individually to the cavity mode (c) Full coupling Hamiltonian. The two ensembles are coupling cooperatively to the cavity mode. The coupling strength is enhanced by a factor  $\sqrt{2}$ . The gray lines correspond to the uncoupled eigenvalues.

spectrum. Due to high losses in this ensemble, the avoided crossing looks blurry and is smeared out. Concerning the second ensemble the strong coupling regime to the cavity mode is found to be between  $60^\circ$ - $80^\circ$  resulting in another avoided level crossing.

At a magnetic field angle of  $48.1^\circ$ , the two ensembles are in resonance with each other and resonant with the cavity mode. The avoided crossing observed corresponds to the eigenstates  $|+\rangle$  and  $|-\rangle$  (see eq. (6.1)). In reference to the theory, the third state  $|0\rangle$  is an antisymmetric Dicke state. This state is invisible in the transmission spectrum since it does not couple to the resonator (dark state). Only a fully symmetric Dicke state couples coherently to the cavity mode. The new fully symmetric Dicke state is formed by a superposition of an excitation in both ensembles. In fig. 6.5 this coupling scheme is graphically represented, and the hybridization of the states is shown.

Figure 6.7 shows several cuts through fig. 6.6 (a) at different field angles (indicated as grey vertical dashed lines in the surface plot). The cavity transmission derived in eq. (3.43) was fitted to the data. The deviations between fit and data have their origin in a Fano resonance of the device. This Fano was not included into the fit. In the frequency domain of interest (avoided crossing), the fit is sufficient to derive the necessary parameters.

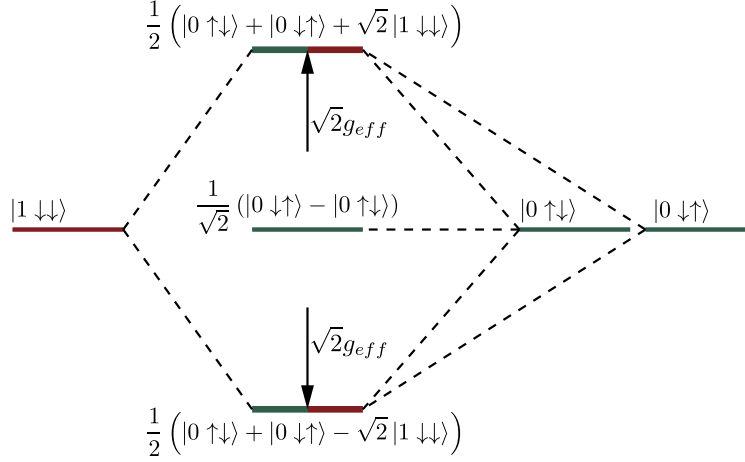


**Figure 6.5:** If all energies are in resonance with each other, a new fully symmetric Dicke state emerges. This Dicke state couples to the cavity mode with an  $\sqrt{2}$  enhanced coupling strength. The antisymmetric Dicke state does not couple to the cavity mode and remains as dark state. The resulting spin wave is de-localized throughout the two separated ensembles.

The collective coupling strength of the two ensembles to the cavity mode can be determined from the cavity transmission at  $48.1^\circ$ . It scales with  $\sqrt{2}$  of the mean coupling strength of the two ensembles ( $\sqrt{2} \cdot \frac{g_{eff1} + g_{eff2}}{2}$ ) to the cavity mode.

In this scheme it is possible to consider the system as an effective giant spin ensemble that coherently interacts with the cavity mode in the strong coupling regime. All single ensemble-cavity calculations therefore become valid for this configuration of the system.

In the measurement results shown in fig. 6.8 (a) the degeneracy point of the two spin transitions was tuned below the cavity resonance. By using a wider probe span than in fig. 6.6 (a) it is possible to directly observe the tuning of the two spin transitions (faint features in the frequency domain 2.765 GHz to 2.79 GHz).

The system offers a huge advantage. The two ensembles can be individually coupled to the cavity mode. By means of the rotational degree of freedom the two ensembles can also be tuned into degeneracy. They merge to a single giant ensemble, which makes a distinction between the spatially separated ensembles impossible and the coupling strength increases by a factor  $\sqrt{2}$ . This directly shows the coherency of the coupling to the cavity mode. Another interesting feature can be observed when taking a look at the different loss parameters in table 6.2. The loss parameter of the giant coupled ensemble is given by the loss parameter of ensemble 2. The cavity exhibits a protection effect on the giant ensemble which has its origin in the stronger coupling strength to the cavity mode. Information about this effect can be found in a paper by Putz et. al. [PKA<sup>+</sup>14].



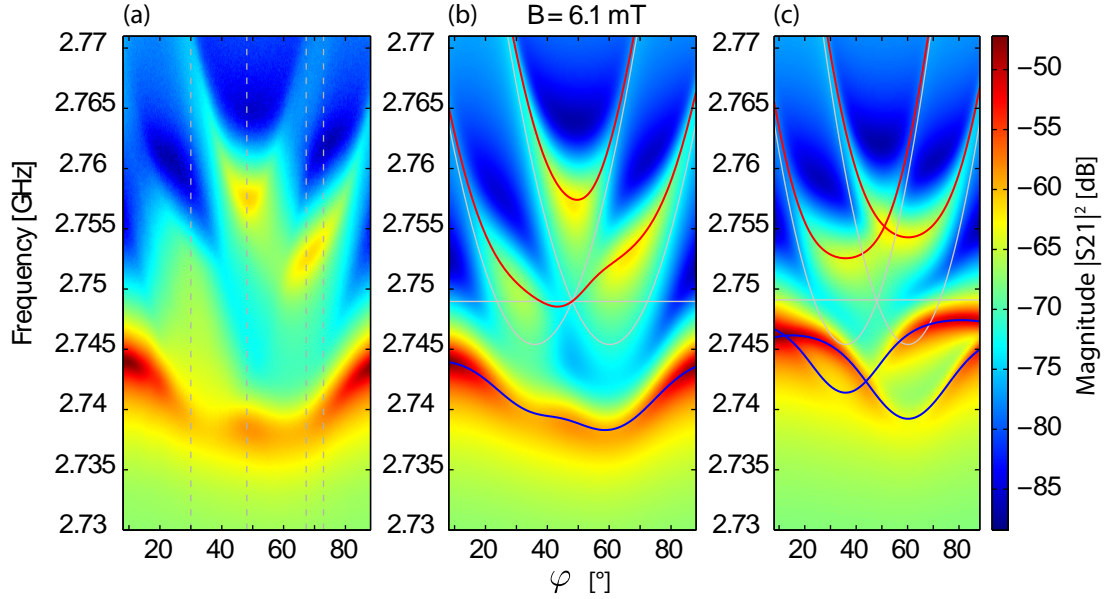


**Figure 6.6:** Measurement result of the direct coupling of two ensembles to the cavity mode. The cavity transmission spectrum was probed with a VNA. The plot shows the  $S_{21}$  scattering parameter. Colors correspond to the transmission in  $dB$ . The magnitude of the magnetic field is kept constant  $B=6.1$  mT and rotated in the (001) crystal plane from about  $10^\circ$  to  $90^\circ$ . Dashed lines in (a) correspond to fig. 6.7.  $T=70$  mK.

	ensemble 1 $16^\circ$ [MHz]	ensemble 2 $79^\circ$ [MHz]	collective $48.1^\circ$ [MHz]
$\frac{g}{2\pi}$	6.25	7.65	9.66
$\frac{\gamma}{2\pi}$	11.5	6	6

**Table 6.2:** Coupling strength and loss parameter of the two different ensembles used in the experiment.

### 6.1.2.2 Parameters of the two ensembles

The parameters of the individual diamonds can be determined separately via a spectroscopy of the cavity transmission versus the magnetic field under a constant field angle. At this point the reader is referred to appendix B, where these measurements of how to obtain the following parameters are shown.

The loss parameter and the coupling strength of the collective ensemble and of the individual ensembles are of special interest since they are used in the simulations of the system. Therefore, they are listed in table 6.2 together with the constant magnetic field angle.

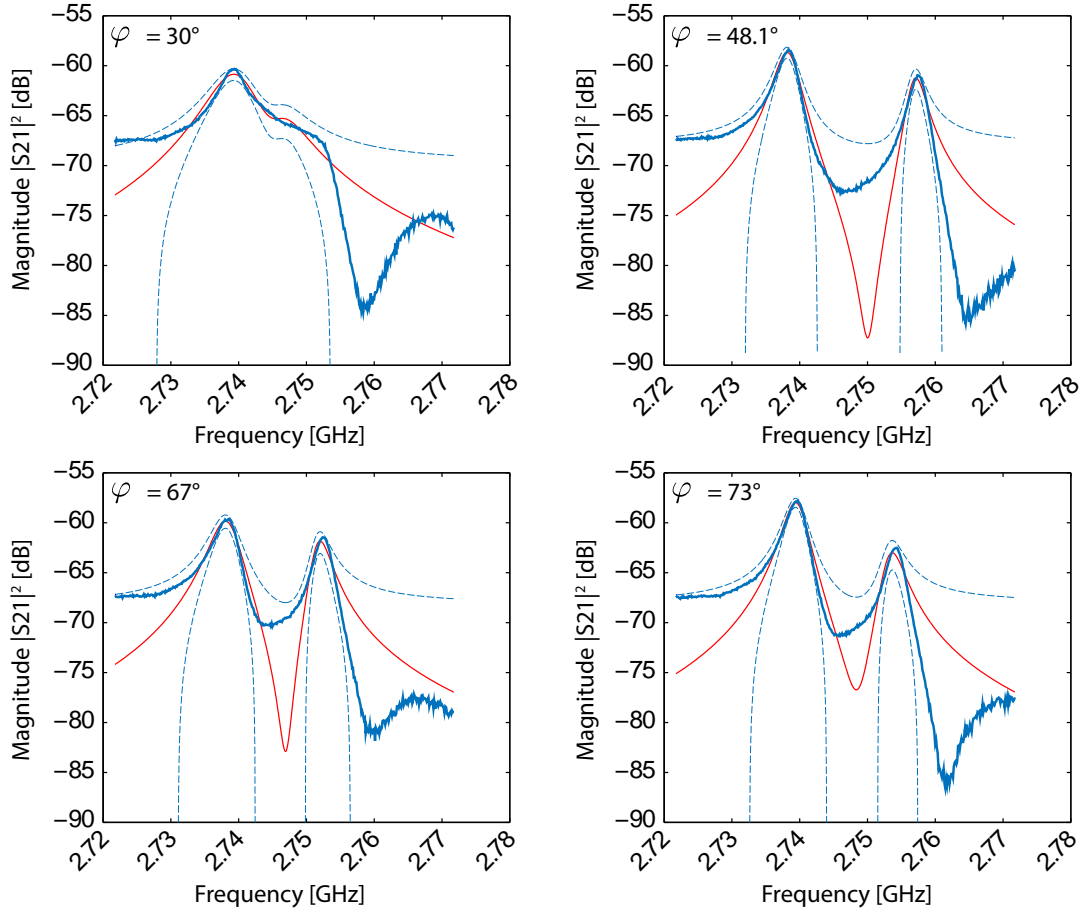


**Figure 6.7:** Spectroscopy signal for different field angles at a constant field magnitude of 6.1 mT. The transition energies of both ensembles are perfectly aligned with the cavity frequency. The data was fit with the calculated cavity transmission, see eq. (3.43). The solid blue line corresponds to the magnitude of the  $S_{21}$  parameter. The red line is the fit to the data. The dashed blue lines indicate the 95% prediction bounds of the fit. All data points are within these bounds.

### 6.1.2.3 Simulation

In fig. 6.6 (b) The cavity transmission data in fig. 6.6 (a) and fig. 6.8 (a) has been simulated by scattering matrix theory [Dys49]. To derive the transmission spectrum, the inverse of the systems Green function is computed. Necessary parameters are losses (cavity and spin), the cavity transmission frequency and an additional Fano resonance of the device. With this simple model it is possible to give a valid description of the basic physics of the system. The simulations are shown in fig. 6.6 (b) and fig. 6.8 (b).

A simulation of the system in case of an incoherent coupling of the two ensembles with the cavity is shown in fig. 6.6 and fig. 6.8 (c). In this term 'incoherent' refers to a coherent coupling of a single ensemble to the cavity mode, but no enhancement of the coupling

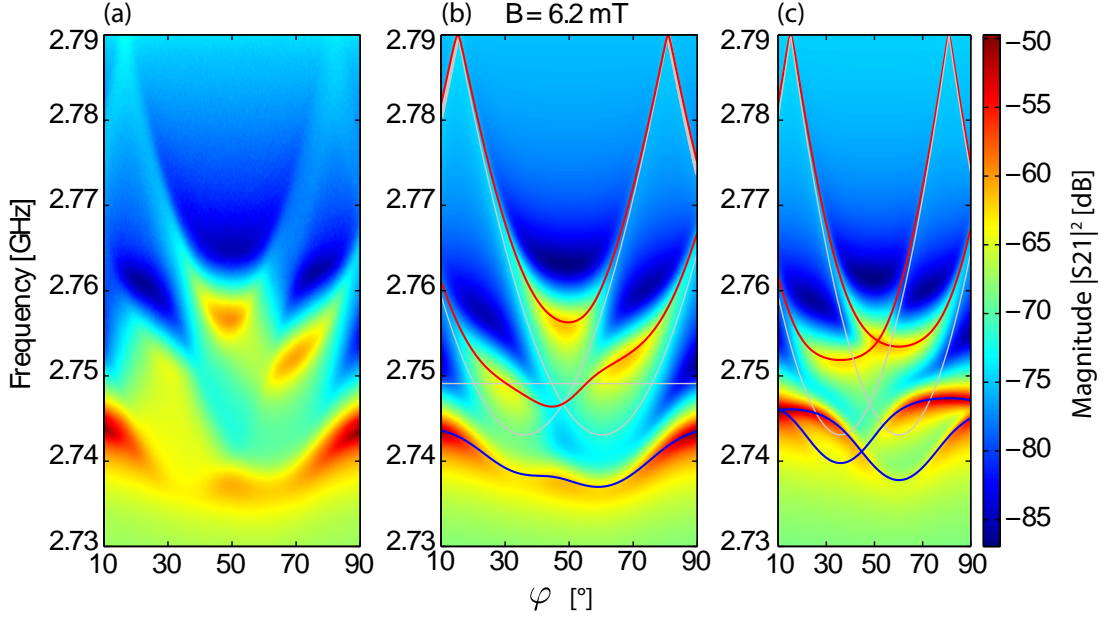


**Figure 6.8:** (a) Cavity transmission spectroscopy for a constant magnetic field amplitude of 6.2 mT. From (b) it can be seen that the two spin transitions are in resonance slightly below the cavity frequency ( $48.1^\circ$ ). Furthermore, (b) shows the uncoupled transition energies and cavity frequency (solid grey lines). The coupled system is indicated by red solid lines. The blue solid line represents the cavity frequency. (c) Incoherent sum of the transmission spectra for each ensemble (simulation).

strength by a factor  $\sqrt{2}$ . The plot arises from the incoherent sum of the transmission spectra of each ensemble simulated independently.

## 6.2 Dispersive regime

The regime in which the spin transitions are far detuned from the cavity is called dispersive regime ( $\Delta_{det} = |\omega_c - \omega_s| \gg (g_{eff}, \kappa/2, \gamma/2)$ ). From the theory it is known that in the dispersive regime the spin system has an influence on the cavity resonance frequency. The cavity resonance frequency is shifted to lower/higher frequencies, depending on the relative position of the ESR transition. The first order correction of the cavity resonance is given by  $\Delta_{disp} = \pm \frac{g_{eff}^2}{\Delta_{det}} \langle S_z \rangle$ . This frequency shift can be undone by pumping spin population from the  $|\downarrow\rangle$  ground state to the excited  $|\uparrow\rangle$  state. A strong microwave continuous wave signal is applied to the system in order to drive the transition. If the pump tone is close to or hits the transition, population is pumped. By doing a spectroscopy with the pump signal over a defined frequency region, the transition energies can be mapped to the measured data.

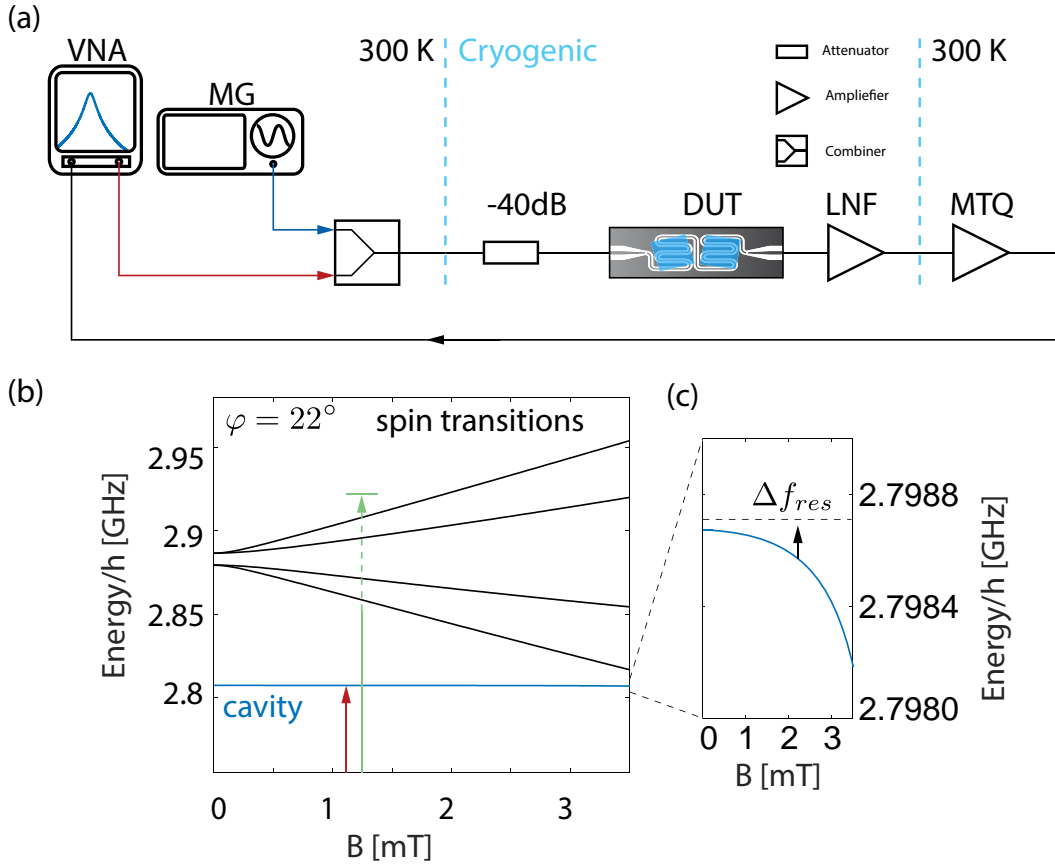


**Figure 6.9:** (a) Schematic of the experimental set-up for experiments in the dispersive regime. A microwave source provides a strong pump signal to pump spins into the excited state. (b) Energy levels versus magnetic field. The green arrow indicates the pump signal which drives the transition. The pump signal is scanned through a certain frequency region. The cavity can still be probed with a signal from the VNA (red arrow). (c) Enlarged view of the cavity response to the presence of the spin transitions. The closer a transition is to the cavity, the more the cavity gets pushed to lower frequencies.

The cavity acts as a very narrow bandwidth filter, so most part of the microwave signal is reflected and only part of it is coupled into the device. To have enough energy in the device, an output power of 15 dBm at the source was used. This power turned out to be a compromise between being high enough for population pumping but low enough to avoid any heating of the system. Figure 6.9 shows the basic measurement set-up to do experiments in the dispersive regime.

### 6.2.1 Initial relaxation

Empirically, 70 mK was found to be an optimal temperature for dispersive two tone experiments. The polarization of the spins in the ground state is still high enough<sup>3</sup> and the ADR cooling energy can be dosed in a way that it is possible to stabilize the temperature up to 12 hours, depending on probe tone power and microwave power applied to the system.

In the first attempts of dispersive measurement sequences it was not possible to get a valid signal. It turned out that the system shows a slow relaxation process after being cooled down from 2.7 K to 70 mK. So far, it is not possible to determine the origin of this relaxation process.

#### 6.2.1.1 Measurement result

The transmission spectrum of the cavity was taken every 7 seconds over a few hours. The data was fitted with a Lorentzian line shape to determine the describing parameters and their behavior over time. One can speculate if this relaxation is related to the spin ensemble, that is relaxing into the ground state, or if the lattice itself is responsible. The other speculation is that the ADR FAA material still relaxes and produces this effect on the cavity. Figure 6.10 shows the behavior of the cavity resonance frequency and quality factor over time. After approx. 5000s after temperature stabilization, the resonance frequency can be considered constant in terms of stability needed for dispersive experiments. This waiting time, however, reduces the time frame available for measurements significantly.

### 6.2.2 Dispersive shift background correction

To find the transition energies for the coupled system and an arbitrary magnetic field amplitude and angle, it is necessary to numerically diagonalize the full Hamiltonian. Figure 6.11 shows an angle resolved plot of the transition energies. The field amplitude has been chosen so low, that the system is in the dispersive limit ( $B=5.4$  mT). As seen in fig. 6.11, the dispersive cavity shift changes for all angles  $\varphi$  (and amplitudes) of the magnetic field.

To define a zero line for dispersive experiments, the cavity resonance frequency has to be determined for all angles of interest at a certain field amplitude. In fig. 6.12 the

---

<sup>3</sup>Calculations were made by Robert Amsuess in his PhD thesis. He states a relative magnetization of 84% at 50 mK and 51% at 100 mK [Ams13].

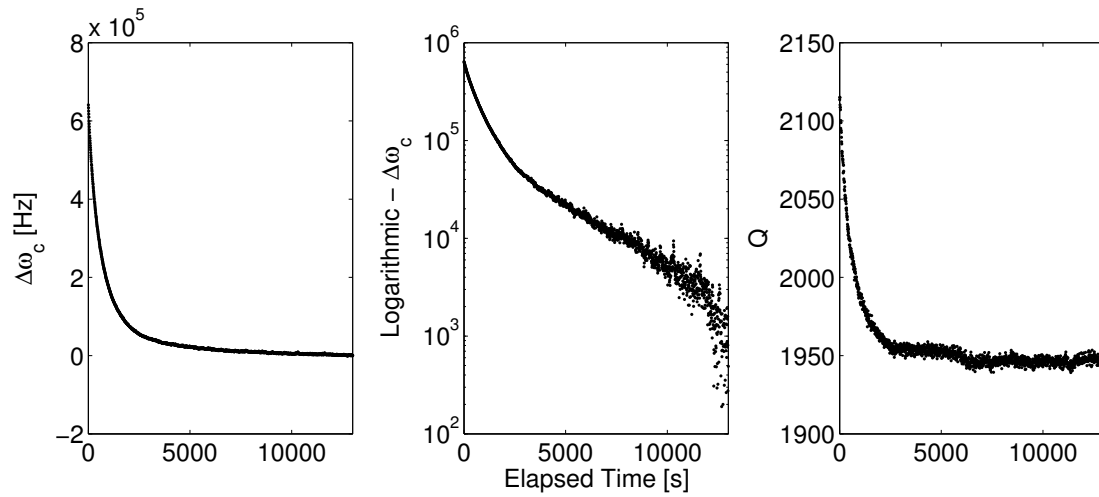


**Figure 6.10:** Relaxation process of the cavity. The resonance frequency of the cavity slowly shifts to lower frequencies with time. Also the quality factor is affected from this process and decreases. The temperature was kept constant at 70 mK for the time of the measurement.

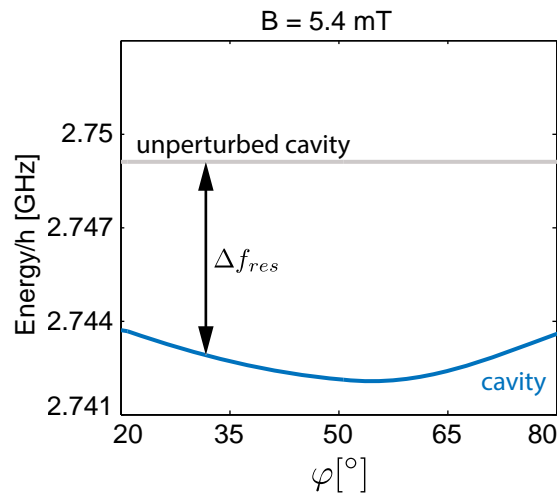


**Figure 6.11:** Dispersive cavity shift: The spin transitions are far detuned from the cavity. The presence of the spin system shifts the cavity to lower frequencies. For a certain magnetic field amplitude the dispersive shift is dependent on the angle at which the magnetic field is applied.

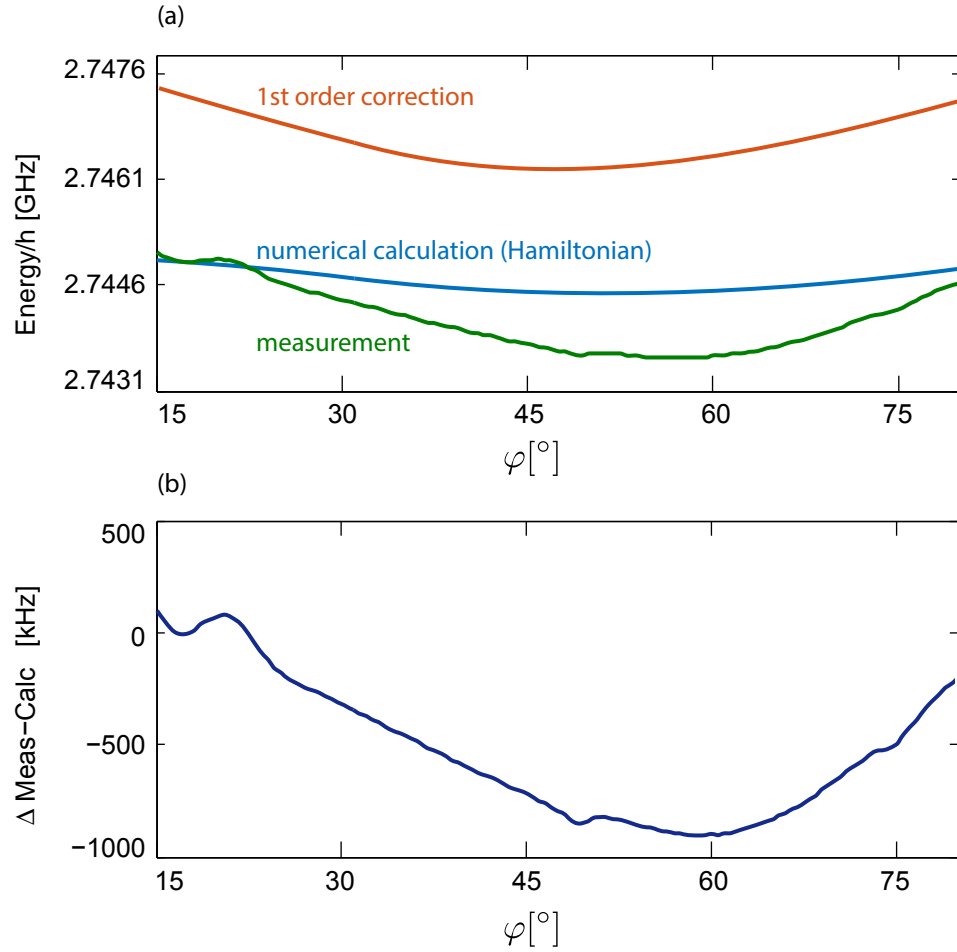


**Figure 6.12:** Background correction for a magnetic field amplitude of 5.4 mT (a) Measured cavity shift for different field angles (blue line). The measurement is compared to the first order correction (orange) of the cavity frequency and to a numerical diagonalization of the Hamiltonian (blue). (b) Difference between the numerical cavity frequency and measured cavity frequency.

measured and calculated cavity shift for two field amplitudes is shown. The obtained data is compared to the calculated cavity frequency from the Hamiltonian and to the first order approximation of the cavity shift ( $\omega_{shifted} = \omega_c - \frac{g_{eff}^2}{\Delta_{det}}$ ). In the lower subplots the difference between measurement and numerical diagonalization of the Hamiltonian is plotted.

Neither the value obtained from the Hamiltonian nor the first order approximation gives a sufficient description of the measured cavity shift. A third order polynomial was fitted to the data, which allowed an adequate correction of the background for all further measurements. The inaccuracy of the calculated background may have its origin in the incompleteness of the model (coupling to nearby  $^{13}\text{C}$ ) and the uncertainty of several parameters (coupling strength, losses, etc.).

### 6.3 Transversal coupling - J coupling

Using two superconducting qubits, several groups have shown that it is possible to coherently couple them with each other and even perform quantum gate operations [YPA<sup>+</sup>06], [HRP<sup>+</sup>06], [QQ03]. In the paper by Majer et. al., a transversal coupling of two transmon qubits coupled to a transmission line resonator was successfully realized. They present fast control of the qubits and coherent quantum state transfer between them.

Furthermore, it has been shown that an ensemble qubit can successfully be used to store and retrieve quantum information [SZA<sup>+</sup>13]. The superior T1 times of the system, which will be presented in the next section, indicate the suitability of cavity-ensemble systems as quantum memory.

The transversal coupling of two macroscopically ensemble qubits has not yet been demonstrated. It allows a coupling of the two ensembles even without populating the cavity bus with real photons. The architecture can easily be expanded to more than a two ensemble qubit device, maintaining control of the coupling of two individual ensemble qubits. Consequently, a transversal coupling of the two ensemble qubits offers huge potential for further applications in quantum information technologies.

#### 6.3.1 Measurement

In this measurement sequence the pump tone frequency is swept through the region of interest and the relative cavity shift is recorded. Whenever the pump tone matches the ESR transition of the  $NV^-$  sub ensemble, population is pumped from the ground state  $|\downarrow\rangle$  to the  $|\uparrow\rangle$  state. The cavity then shifts to higher frequencies. By rotating the magnetic field and repeating the pump sequence, the  $NV^-$  transitions can be identified and mapped to the calculated transition energies. In all these measurements the transition energies are far detuned from the cavity.

Difficulties regarding this measurement scheme arise in the data acquisition, which is very time consuming due to the long spin lattice relaxation time. To ensure that both ensembles are in the ground state before applying the pump tone again, the system was given several hundred seconds to relax.

In the experiment the  $|\downarrow\rangle \rightarrow |\uparrow\rangle$  transition of both ensembles was tracked over a wide range of different magnetic field angles (amplitude constant). As mentioned in previous sections, the transition energies of both ensembles match at  $48.1^\circ$  and an avoided level crossing even in the dispersive regime is expected. However, the calculated coupling



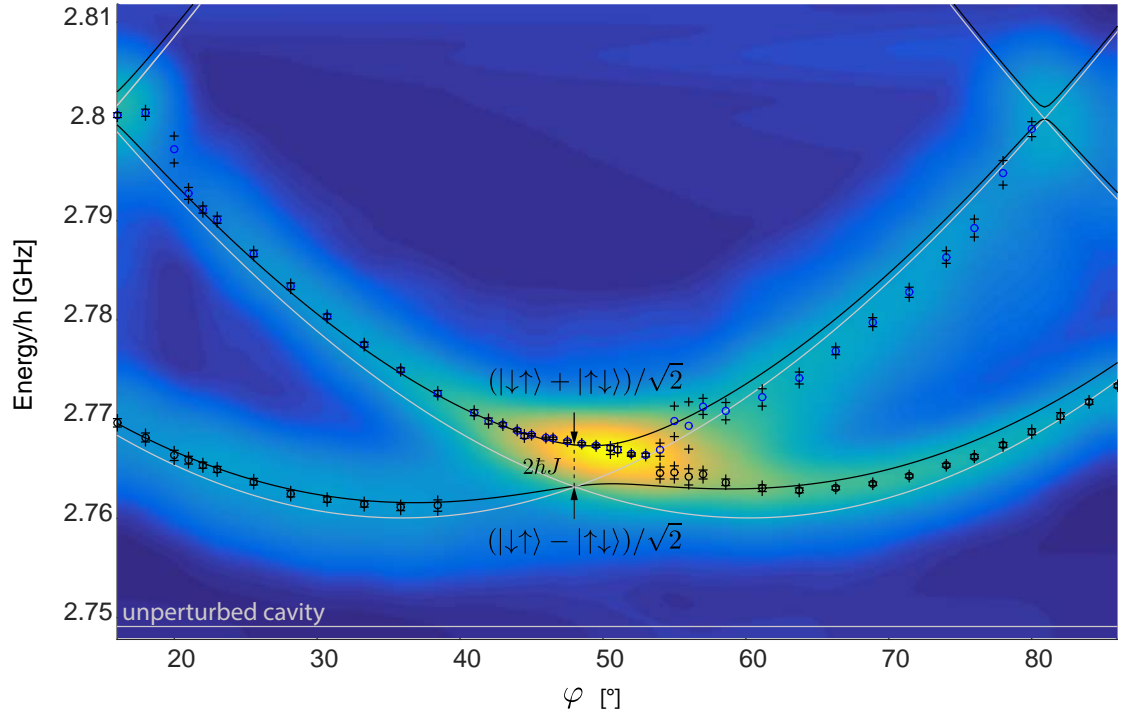


**Figure 6.13:** The figure shows an angle resolved spectroscopy in the dispersive regime. The  $z$  direction is given by the dispersive cavity shift. Between  $40^\circ$  and  $50^\circ$  the lower branch (lower black line) shows the discussed dark states.

between the two ensembles is just in the order of 2 MHz. The line widths of the two ensembles are in the order of 10 MHz and 6 MHz. Consequently, it is not possible to resolve the avoided crossing in the dispersive regime. Inhomogeneous broadening (further discussed in section 6.3.4) is one of the main source for decoherence in this system. It limits the possibilities of coherently transferring and storing quantum information. In a paper by S. Putz et. al. [PKA<sup>+</sup>14], it is shown how inhomogeneous broadening can be efficiently suppressed in the strong coupling regime - an effect that is called 'cavity protection'.

Figure 6.13 shows a surface plot of the obtained data. The measured angle span has been divided into 86 slices. The data in between has been interpolated and smoothed, using a tool by Garcia. He provides a fully automated smoothing procedure for gridded data in one and higher dimensions with missing values [Gar10].

### 6.3.2 Transversal coupling mechanism

For the transversal coupling a slightly different Hamiltonian than the already discussed Tavis-Cummings Hamiltonian shall be introduced. In [BGW<sup>+</sup>07] it is shown how a

direct qubit-resonator coupling can be eliminated in the dispersive regime with a transformation. Subsequently, a similar Hamiltonian for this system can be built [FGF<sup>+</sup>11a]:

$$H_J = \hbar \left( \omega_c + \chi^{(1)} \sigma_z^{(1)} + \chi^{(2)} \sigma_z^{(2)} \right) a^\dagger a + \hbar \sum_{i=1,2} \frac{\omega_{\downarrow\uparrow} + \chi^{(i)}}{2} \sigma_z^{(i)} + \hbar J \left( \sigma_+^{(1)} \sigma_-^{(2)} + \sigma_+^{(2)} \sigma_-^{(1)} \right) \quad (6.2)$$

The underlying method behind is the adiabatically elimination of the direct ensemble resonator coupling. The first term in eq. (6.2) describes the cavity mode  $\omega_c$ , together with the dispersive cavity shift  $\chi^{(i)} = (g^{(i)})^2 / \Delta_{det}$  for each ensemble<sup>4</sup>. The second term comprises the Lamb shift  $\chi^{(i)}$ , which modifies the transition energy of each ensemble. In the paper by Fragner et. al. [FGF<sup>+</sup>08], it is reported that the lamb shift is in the order of up to 1.4 % of their qubit transition frequency.

The third term mediates the effective ensemble-ensemble coupling (flip-flop interaction) in this regime via virtual photon exchange. It describes the transversal coupling, which is often referred to as J coupling. The coupling strength J is given by

$$J = \frac{1}{2} g^{(1)} g^{(2)} \left( \frac{1}{\Delta_{det}^{(1)}} + \frac{1}{\Delta_{det}^{(2)}} \right) \quad (6.3)$$

.

The previously discussed Hamiltonian leads to an avoided level crossing of the excited  $NV^-$  states of the system. By looking at the eigenstates of the system, one finds the new eigenstates as the symmetric dublett states  $|\downarrow\downarrow\rangle$  and  $|+\rangle_s = 1/\sqrt{2}(|\downarrow\uparrow\rangle + |\uparrow\downarrow\rangle)$ , as well as the antisymmetric singlet state  $|-\rangle_a = 1/\sqrt{2}(|\downarrow\uparrow\rangle - |\uparrow\downarrow\rangle)$ . The system shows maximal entanglement in the  $|\pm\rangle_{s/a}$  state, which can be seen as a single excitation shared by both ensembles. These states do not incorporate any population of the cavity. Therefore, it is possible to suppress all cavity related loss channels.

In fig. 6.14 a graphical representation of the J coupling scheme is given (a). In (b) the hybridization of the resulting states is shown.

### 6.3.3 Dark states

A characteristic of the avoided crossing is the appearance of a dark resonance. A transition from the ground state to this state is forbidden. In the measurement the pump signal does not affect the system. Consequently, no cavity shift can be observed. In

<sup>4</sup>Here the index i corresponds to the two ensembles separated from each other, including their sub-ensembles.

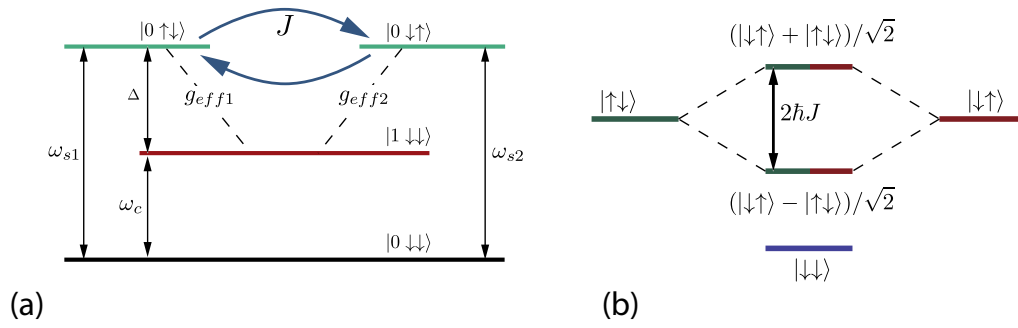


**Figure 6.14:** (a) Dispersive ensemble-ensemble coupling scheme. The two ensembles are in resonance with each other but far detuned from the cavity. The excited states of the two ensembles interact via a virtual cavity photon. (b) Hybridization of the states in the dispersive limit.

a paper from S. Filipp [FGF<sup>+</sup>11b] as well as J.Majer [MCG<sup>+</sup>07], they state that the origin of this dark state lies in a selection rule which arises from the symmetry of the dispersive pump drive. At the avoided crossing, the eigenstates are a superposition of the two excited ensemble states. The external drive applied to the system is not able to drive any transitions to the antisymmetric state. Therefore, it is observed to be a dark state in the spectroscopy. For further information on this topic, the reader is referred to [FGF<sup>+</sup>11b], [BGW<sup>+</sup>07] and [MCG<sup>+</sup>07].

Figure 6.13 presents the dispersive spectroscopy spectrum of the coupled  $NV^-$  system. The figure shows the dispersive cavity shift in z direction with respect to the pump signal and angle of the magnetic field. Between  $40^\circ$  and  $48^\circ$  the spectroscopy signal (cavity shift) of the lower branch vanishes, which gives rise to the discussed dark state. Unfortunately, it is not possible to directly observe the avoided level crossing in the dispersive regime since the spin losses are higher than the coupling strength  $J$  between the two ensembles. However, the coherence of the coupling of the two ensembles manifests itself in the observed dark state, which proves the transversal coupling between the ensembles.

### 6.3.4 Effects of inhomogeneous broadening

The discussed system can be seen as an ensemble of independent spin-one particles. The creation process of  $NV^-$  from the existing P1 centers <sup>5</sup> has only an efficiency in the order of 1% to 10%. The remaining P1 centers contribute to the line-width of the spin transition via dipole-dipole interaction [TCC<sup>+</sup>08]. Moreover, the natural presence of  $^{13}C$  also contributes to the line broadening of the spin transition. In the paper by

<sup>5</sup>The P1 center describes a dominating defect of the diamond crystal. It consists of a single substitutional nitrogen atom. The nitrogen forms four hybrid bonds with the nearest carbon atom.

K. Sandner [SRA<sup>+</sup>12], an analysis of the inhomogeneous frequency distribution can be found. They further state that the spin distribution can be described with a q-Gaussian line shape. The q-Gaussian distribution arises from a generalization of the Gaussian distribution and is given by

$$f(x) = A \left[ 1 - \frac{(1-q)(x-x_0)^2}{w} \right]^{\frac{1}{1-q}}, \quad (6.4)$$

with the parameters amplitude ( $A$ ), peak position ( $x_0$ ), peak width ( $w$ ) and the  $q$  parameter.

In the dispersive level spectroscopy this q-Gaussian function was used to fit the data and determine the position of the transition and its width. The  $q$  parameter has been set to the value  $q = 1.38$  which has been determined in the paper by K. Sandner. Figure 6.15 shows several cuts through the surface plot of fig. 6.13. The position of q-Gaussians is plotted in fig. 6.13 (marker with error crosses). The obtained data points are in good agreement with the theory predictions (black lines in fig. 6.13). It is not possible to fit two peaks in the range between  $40^\circ$  and  $60^\circ$  due to the dark state.

## 6.4 Spin lattice relaxation

The  $T_1$  relaxation time is a measure for the longitudinal relaxation process of the system. It is a limiting factor of coherence in the system. Excited spins have a certain probability of relaxing to their ground state. Underlying processes are spontaneous emission, spin-phonon interaction and other spin-flip interactions. These processes appear stochastically and perturb the wave function, which ultimately leads to decoherence.

$T_1$  times that are several orders of magnitude longer than with transmon qubits have been already shown by Amsuess et. al [AKN<sup>+</sup>11] in an  $NV^-$  ensemble. Together with the characteristic scaling of the coupling strength of an ensemble with  $\sqrt{N}$ , these qubits are promising and attractive candidates for quantum information processing on integrated circuits.

This section deals with the determination of the spin lattice relaxation time  $T_1$  of two different spin ensembles with no external magnetic field present. The underlying decay type of the  $T_1$  relaxation process and an overall temperature dependence of  $T_1$  will be investigated.

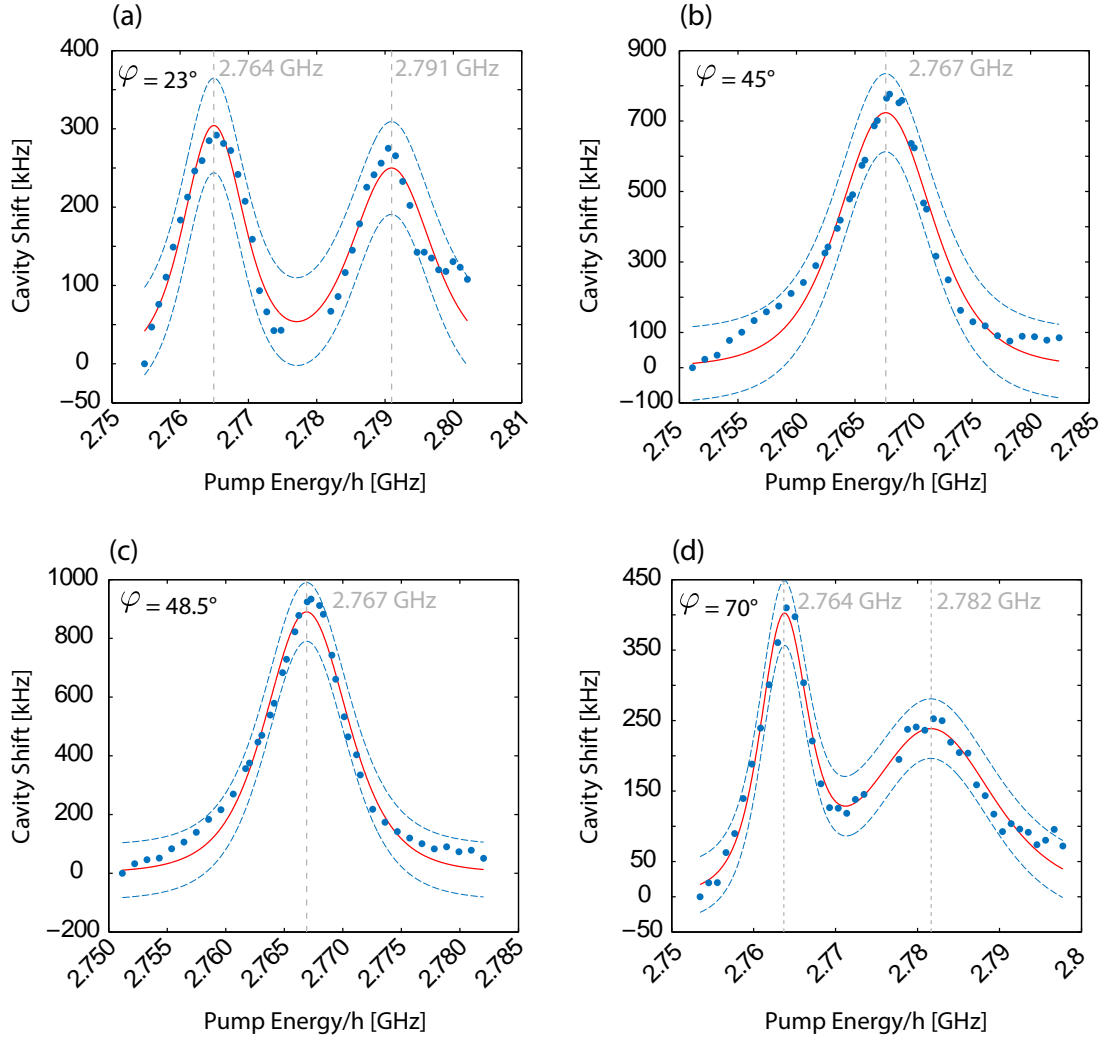


**Figure 6.15:** Different cuts through the dispersive level spectroscopy (see fig. 6.13) at different angles. (a)  $\varphi = 23^\circ$ : The transition energies of the two ensembles are clearly distinguishable and can be fitted with two q-Gaussian functions to determine peak position and width. (b)  $\varphi = 45^\circ$ : Because of the coupling of the two ensembles and the resulting dark state, only one peak remains. A single q-Gaussian function was fitted to the data. (c)  $\varphi = 48.1^\circ$ : The transition energies of both ensembles are resonant and only the symmetric state  $1/\sqrt{2}(|\uparrow\downarrow\rangle + |\downarrow\uparrow\rangle)$  can be seen in the spectroscopy. (d)  $\varphi = 70^\circ$ . Again two distinguishable spin transitions corresponding to the two ensembles are clearly visible in the spectroscopy signal.

### 6.4.1 Dispersive measurement - $NV^- |0\rangle \rightarrow |\pm 1\rangle$

From a dispersive spectroscopy ( $B = 0$ ), the frequency of the  $|0\rangle \rightarrow |\pm 1\rangle$  transition of a single ensemble was determined. In the T1 measurement sequence, a strong drive signal is applied on this transition <sup>6</sup> for 150 s. It sufficiently pumps population from the ground state to the excited state. The effect caused by this pumping can be detected through the cavity shift. The cavity is probed continuously with a probe signal. The power of the probe signal is weak compared to the drive signal in order to avoid any influences on the system by the probe field. After the pump procedure, the pump signal is switched off and the cavity is probed continuously for 450 s.

In the dispersive measurement the diamond sample H1 on a  $\lambda/2$  resonator no. 121 was used. The sample contains  $NV^-$  centers, which were created by neutron irradiation.

#### 6.4.1.1 Stretched exponential decay

In the paper by Amsuess et. al. [AKN<sup>+</sup>11] a the spin relaxation was found to be a single exponential decay process with a relaxation constant  $\tau \approx 45$  s, which is in good agreement with other values found by Harrison et. al. [HSM06].

In contrast to all expectations, the decay mechanism showed a stretched exponential behavior. The stretched exponential is known and used in many different relaxation processes, such as disordered and quenched electronic and molecular systems [Phi99]. In a paper by Johnston et. al. [JBZ<sup>+</sup>05], it is shown that small concentration of magnetic defects in the structure of  $^7Li$  drastically changes the nuclear magnetization relaxation from a pure exponential to a stretched exponential. Moreover, it is stated that this stretched exponential originates from a distribution of nuclear spin-lattice relaxation rates in  $^7Li$ .

The function itself emerges from a generalization of the exponential function by inserting a fractional power law into the exponent. In the standard notation the function has the following form

$$f_\beta(t) = e^{-(t/\tau)^\beta}, \quad (6.5)$$

with  $\beta$  being the stretching exponent. By setting  $\beta = 1$ , one obtains the basic exponential function. Setting  $\beta = 2$ , the normal distribution is found. Consequently, the characteristic stretching appears with  $\beta$  between 0 and 1.

---

<sup>6</sup>Note that the spin transition is far detuned from the cavity

T [mK]	$T_1$ [s]	$\sigma$ [s]
70	80	5.9
80	76	3.5
90	74	3.5
100	71	4.8
110	75	9.9

**Table 6.3:** Measured T1 relaxation time for different temperatures. The temperature was stabilized at the temperatures given in the table.

The origin of this stretched exponential behavior is still part of ongoing research. Impurities in the lattice may result in a distribution of relaxation rates, or a phonon-spin interaction related processes may contribute to this process but at this point only speculations are made.

In another paper by Johnston a detailed discussion on the case of a system containing independently, exponentially relaxing species with a distribution of relaxation rates can be found [Joh06].

#### 6.4.1.2 Temperature dependence

The relaxation process was analyzed in a temperature region from 60 mK up to 1.2 K. Around 350 mK the T1 time already approached zero and above this temperature, nearly no cavity shift was found. With  $\beta \approx 0.6$  for all measured relaxation curves the stretching parameter was determined to be fairly constant within this temperature range. Figure 6.16 shows the obtained result from a measurement run. It is important to note that the temperature evolved during the measurement. The ADR was stabilized at 60 mK base temperature. After a three hour waiting time the T1 measurement procedure was carried out continuously. After a certain time the cooling energy of the ADR was used up and the base temperature began to rise slowly. In fig. 6.18 the temperature curve during the measurement is shown. During the data acquisition of one decay process (250 s), the temperature drift (and cavity resonance drift) of the system is negligible.

To make sure the temperature drift is not an issue, the ADR has been stabilized at certain temperatures, and after the 3 hour waiting time, the T1 time has been measured until the cooling energy was used up. In table 6.3 the results of these measurements is summarized. In fig. 6.17 a statistical evaluation of the data is presented.

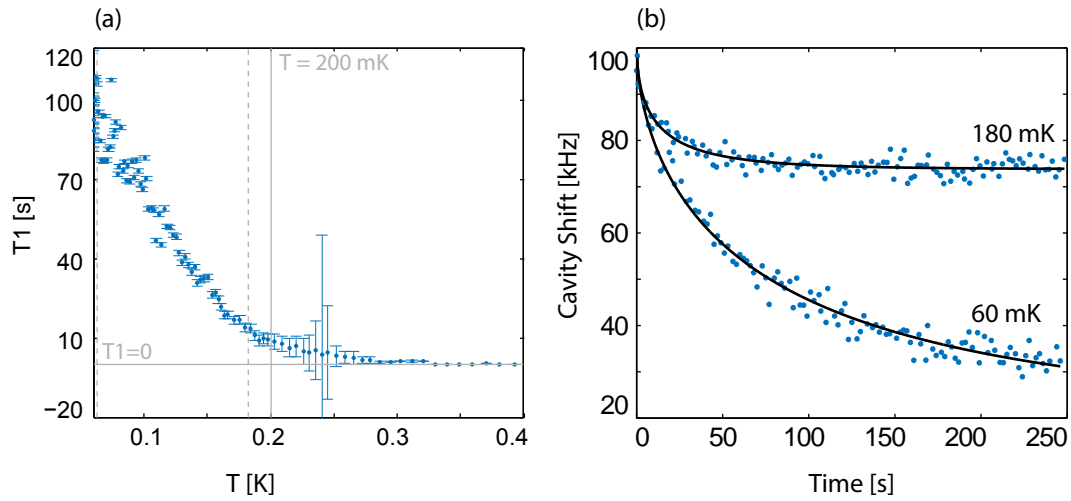


**Figure 6.16:** (a) Temperature dependence of the spin lattice relaxation time  $T_1$ . Measurement of a bare  $NV^-$  transition. The characteristic temperature of 200 mK is marked with a vertical grey line. (b) Sample decay traces taken at two different temperatures. Temperatures correspond to the vertical dashed lines in (a).

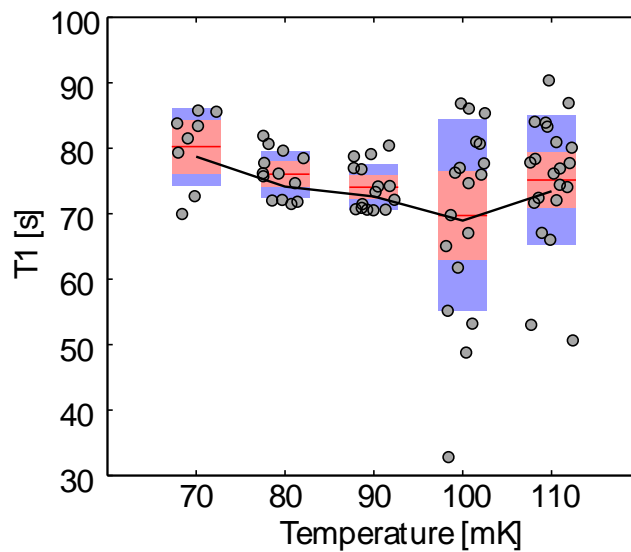


**Figure 6.17:** The figure shows a box plot of the measured  $T_1$  relaxation times. The temperature was stabilized for all measured decay times. A jitter in x direction was added to the data in order to vividly present the data. The black line indicates the mean  $T_1$  decay time of the data points for each temperature.



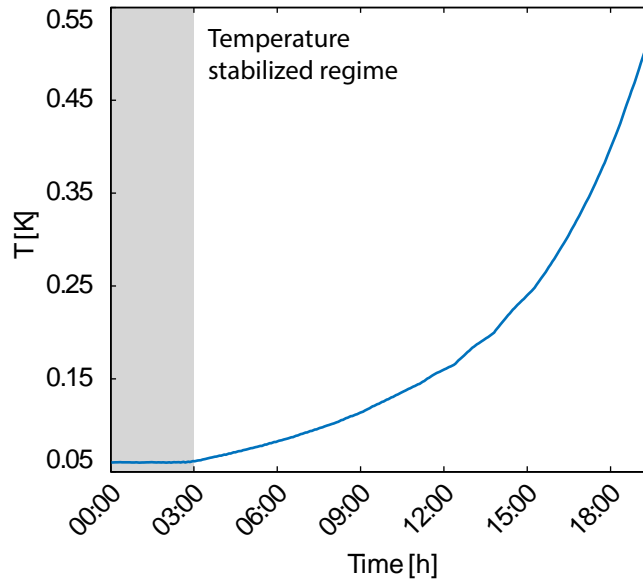


**Figure 6.18:** After a 3 hour waiting time, the temperature can still be maintained at 60 mK for another 3 hours. After that time, the cooling energy is used up and the fridge gradually begins to warm-up.

#### 6.4.2 Resonant measurement - $NV^- - {}^{13}C$ transition

Part of the  $NV^-$  defect centers in diamond are coupled to the naturally occurring  ${}^{13}C$ . Compared to the number bare  $NV^-$  defect centers, the  $NV^- - {}^{13}C$  coupled spins are only a few percent. This hyperfine interaction was already measured by Amsuess [AKN<sup>+</sup>11]. This  $NV^- - {}^{13}C$  sub-ensemble is of particular interest since it offers the first step towards a nuclear ensemble quantum memory. For a more detailed discussion concerning the fine structure of the  $NV^-$  center the reader is referred to [Ams13].

##### Sample and set-up

For this measurement set a transmission lumped element resonator was used. Compared to a  $\lambda/2$  resonator with its distributed elements, the lumped element resonator consists of inter digit fingers acting as capacitor, and meander lines, acting as inductance.

The used diamond sample has electron implanted  $NV^-$  defect centers. The sample itself was received from Berkeley University to investigate differences between T1 of  $NV^-$  diamond samples, which were created by neutron irradiation.

##### 6.4.2.1 Wide range two tone spectroscopy

In order to correctly identify the  $NV^- - {}^{13}C$  transitions, a dispersive two tone spectroscopy was carried out. The cavity shift in the resonant regime can even be used to

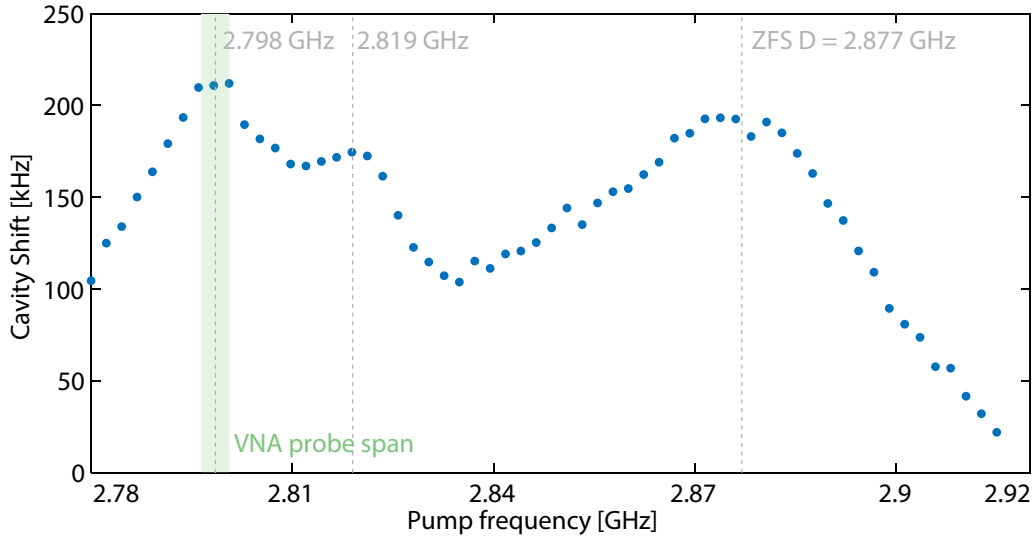


**Figure 6.19:** Wide range two tone spectroscopy to identify different transition energies. The dispersive cavity shift is recorded versus the frequency of the pump signal. The zero field splitting of the  $NV^-$  is weak in this sample. The VNA probe span is shown as the green area. The pump tone strongly affects the cavity in the resonant regime.

identify the different transition energies. Figure 6.19 shows the obtained data from the two tone spectroscopy with several features. The zero field split parameter  $D$  can be found at 2.87 GHz. A  $NV^- -^{13}C$  transition can be found around 2.82 GHz. Slightly below 2.8 GHz a second  $NV^- -^{13}C$  transition can be identified. This transition is already in resonance with the cavity without any external magnetic field. The coupling to this sub ensemble is very weak and no normal mode splitting is visible. However, this presents an experimental advantage.

### Measurement sequence

With the system being in the weak coupling limit, the probe power itself can be employed to pump population from the ground state to the excited state. To measure the  $T_1$  time, the probe tone must be set to very low power in order to avoid any pumping of population.

#### 6.4.2.2 Temperature dependence

The measurement sequence was repeated continuously, starting slightly below 50 mK up to 1.2 K. Cavity shifts in this regime are in the order of almost 250 kHz. Due to this strong signal, no waiting time after cool down was used.

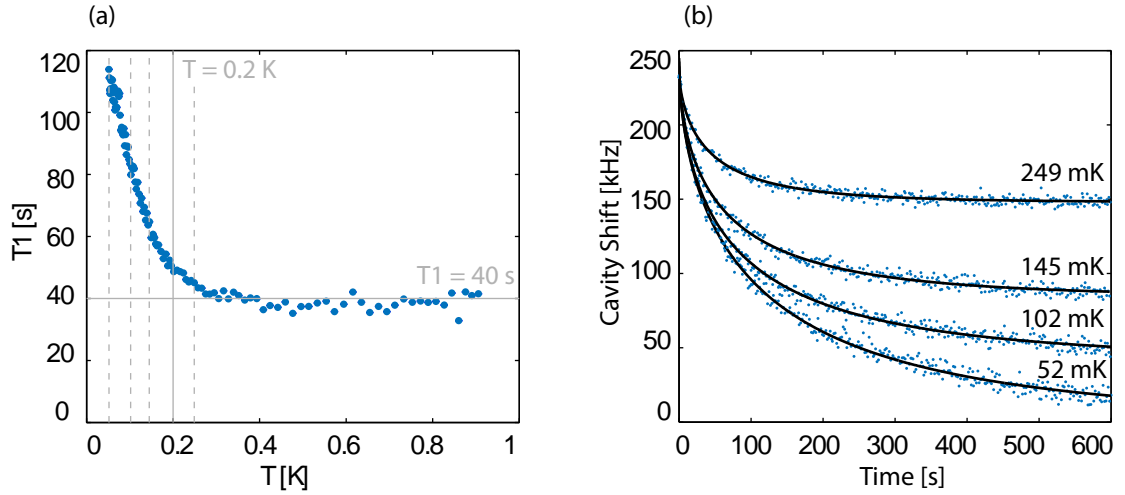


**Figure 6.20:** (a) Temperature dependence of the T1 spin lattice relaxation time. Measured for the  $NV^- - {}^{13}C$  sub ensemble. The T1 time indicates the same characteristics as in the case of a bare  $NV^-$  transition. Around 200 mK the T1 time approaches 40 s. Error bars are all within the marker size. (b) Sample decay traces taken at different temperatures with stretched exponential fit. Temperatures correspond to the vertical dashed lines in (a).

In fig. 6.20 the measured T1 versus temperature curve is shown. This curve shows some similar characteristics as the curve of the bare  $NV^-$  transition discussed in the previous section. Around 200 mK the T1 time suddenly becomes constant over a wide range of temperatures. This behavior is rather unexpected since in the case of the bare  $NV^-$  transition the T1 time starts to become too small to measure after the characteristic temperature of 200 mK.

As the case of measuring T1 times on resonant in a weak coupling regime is rather unconventional, it cannot be ruled out that this type of measurement has an influence on the behavior of the T1 times, or that it possibly alters the data.



## Chapter 7

# Conclusion and outlook

In this thesis a hybrid quantum system with great potential has been presented. The system was built by using a superconducting transmission line resonator, which acts as a high quality quantum bus to transfer and distribute quantum information. Two dense spin ensembles were realized as nitrogen vacancy defect centers in diamond. The coherence of the coupling between the two macroscopically separated ensembles was shown directly in the cavity transmission spectrum with the characteristic  $\sqrt{2}$  scaling of the coupling strength. The two ensembles behave like a giant single ensemble which is strongly coupled to the cavity mode.

Moreover, the transversal J coupling between two ensembles in the dispersive regime was investigated. The appearance of a dark resonance provided proof of the transverse coupling and entanglement of the two ensemble qubits. This coupling mechanism through virtual photons bears the advantage of being able to engineer entangled states of excitations in the two ensembles without populating the cavity.

The evidence of the transversal ensemble coupling opens the possibility to build bigger, coupled ensemble networks on a single chip with the advantage of not introducing additional losses of the cavity bus. External magnetic fields allow the control and switching of the coupling between the ensembles. This hybrid system offers the possibility of adding additional ensemble qubits with the ability of controlling the coupling between them. This shows the excellent scalability of this architecture for further applications in quantum information technology.

As another significant aspect of this quantum system, the spin lattice relaxation time  $T_1$  of a  $NV^- - {}^{13}C$  ensemble versus temperature, was investigated. The system showed excellent relaxation times over a wide range of temperatures. These  $T_1$  times support the robustness of this system for further experiments in cavity quantum electrodynamics.



## Appendix A

### Input impedance calculation

$$\begin{aligned} Z_{in} &= \left[ \frac{1}{R} + \frac{1}{j\omega L} + j\omega C \right]^{-1} = \left[ \frac{1}{R} + \frac{1}{j(\omega_0 + \Delta\omega)L} + j(\omega_0 + \Delta\omega)C \right]^{-1} \\ &= \left[ \frac{1}{R} + \frac{\left(1 + \frac{\Delta\omega}{\omega_0}\right)^{-1}}{j\omega_0 L} + j\omega_0 C + j\Delta\omega C \right]^{-1} \approx \left[ \frac{1}{R} + \frac{\left(1 - \frac{\Delta\omega}{\omega_0}\right)}{j\omega_0 L} + j\omega_0 C + j\Delta\omega C \right]^{-1} \\ &= \left[ \frac{1}{R} - \frac{\frac{\Delta\omega}{\omega_0}}{j\omega_0 L} + \frac{1}{j\omega_0 L} + j\omega_0 C + j\Delta\omega C \right]^{-1} = \left[ \frac{1}{R} \left( 1 - \frac{R\frac{\Delta\omega}{\omega_0}}{j\omega_0 L} + j\frac{\Delta\omega}{\omega_0}\omega_0 CR \right) \right]^{-1} \\ &= R \left[ 1 + j\frac{R}{\omega_0 L} \frac{\Delta\omega}{\omega_0} + j\omega_0 CR \frac{\Delta\omega}{\omega_0} \right]^{-1} = R \left[ 1 + jQ_0 \frac{\Delta\omega}{\omega_0} + jQ_0 \frac{\Delta\omega}{\omega_0} \right]^{-1} \\ &= \frac{R}{1 + j2Q_0 \frac{\Delta\omega}{\omega_0}} \end{aligned} \tag{A.1}$$





## Appendix B

# Individual and collective ensemble parameters

Parameters obtained in a cavity transmission spectroscopy versus magnetic field amplitude for different magnetic field angles.

$\cdot \frac{1}{2\pi}$	ensemble 1 16°	ensemble 2 79°	collective 48.1°
$\Omega$	11.2 MHz	14.8 MHz	19.12 MHz
$\Gamma$	6 MHz	13.4 MHz	3.2 MHz
$g_{eff}$	6.25 MHz	7.65 MHz	9.66 MHz
$\gamma$	11.5 MHz	6.4 MHz	6 MHz

**Table B.1:** Measured data of resonance frequency and quality factor for the unloaded and diamond loaded cavity no. 270.

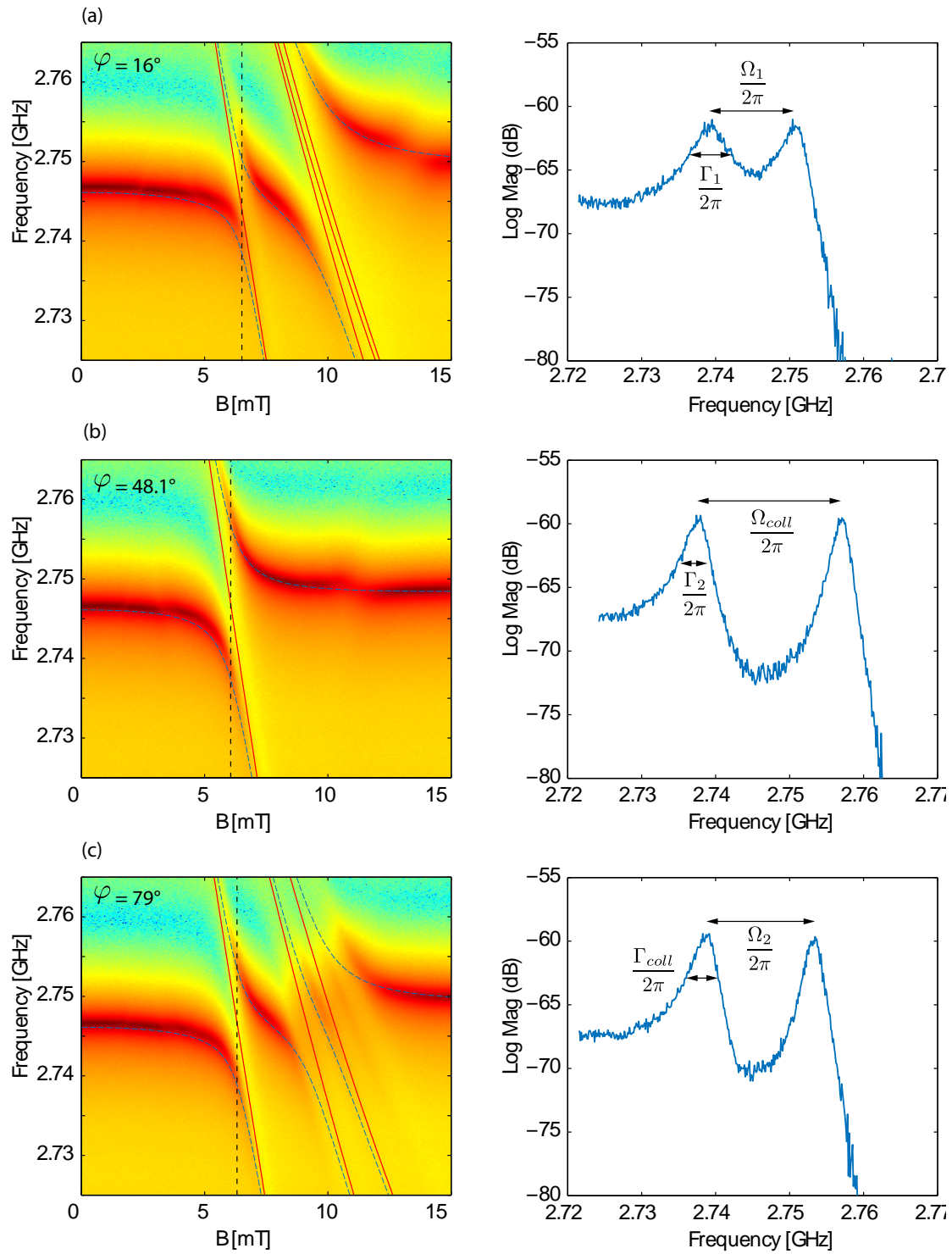


**Figure B.1:** Cavity transmission spectroscopy versus magnetic field amplitude for different field angles. (a)-(c) show the obtained transmission spectrum with a cut through the surface plot. The parameters were determined from the avoided crossing.

## Appendix C

### Lorentzian fit

The frequency response of the used cavity is represented by a Lorentzian line shape. The describing parameters such as transmission amplitude ( $A$ ), quality factor ( $Q$ ) and resonance frequency ( $f_{res}$ ) can be extracted from a fit to the obtained scattering parameters  $S_{21}(f)$ . The VNA measures both transmitted amplitude and phase properties of the probe signal. From eq. (2.2) it is known how to approximate the transmission close to resonance ( $f \approx f_0$ ) with

$$S_{21} = \frac{A}{1 + 2jQ\frac{f-f_0}{f_0}}. \quad (\text{C.1})$$

It is not advisable to fit the square magnitude  $|S_{21}(f)|^2$ . The VNA provides vector network data. Both signals transmitted amplitude and phase properties have normal distributed noise on the signal. The resulting noise of  $|S_{21}(f)|^2$  does not follow the normal distribution. Therefore, it is important to fit the Lorentzian function as a complex function in the following form,

$$S_{21}(f) = Ae^{-i\varphi}e^{ifdt}\frac{-i\frac{\Gamma}{2}}{f - f_0 - i\frac{\Gamma}{2}}. \quad (\text{C.2})$$

In eq. (C.2)  $A$  is the transmitted amplitude,  $f_0$  the cavity resonance frequency, FWHM parameter  $\Gamma$ ,  $\varphi$  a global phase,  $f$  the probe signal frequency and a phase parameter  $dt$ . The fit was implemented in a MATLAB script, using nonlinear least square method. The function tries to find the minimum of the function  $\chi = \sum_i (|S_{21}(f_{meas}^{(i)}) - S_{21}(f_{fit}^{(i)})|^2$ .  $\chi$  is dependent on the number of parameters in the used fit function. The algorithm used has to find the minimum in a multidimensional space, which is only possible if good start parameters are set. Parameters like resonance frequency and FWHM can be easily determined from the data and can be fed to the algorithm. It is important to watch out for correlations between the parameters, which may also result in undesired fit results.



# *Acknowledgements*

I owe this work to countless people. Without the help of them this would have never been finished. For over 1.5 years I am now part of the atomchip group and so I want to mention some of the people here to show my gratitude.

I want to thank,

Jörg Schmiedmayer, the head of the group for enabling us to develop ourselves in so many different ways without any constrictions. I enjoy the atmosphere and freedom in this group.

Hannes Majer, for all the discussions in his office, for his faith in my work and all the endless knowledge that I gained throughout the year with his help.

The doubly 'degenerate' Stefans (Nevlacsil, Putz) together with Ralph and Andreas from the lab. Our discussions were not always easy but ultimately lead to so many new ideas. The people I shared my office with (Stefan, Bernhard, Georg) for helping me with all sorts of day to day issues.

My friends and roomies (Bernhard Jelinek, Isabella Ritzer, Sarah Majcenovic) for sharing life the last years, for being friends and knowing that I can count on them. Sarah, for the professional proof reading of my thesis, although it might have been a bit off your field of interest.

Peter Hofer, for sharing a desk during writing thesis. The hours writing with you were amazingly productive.

The Schluwi, a Beisl which became my second living room, together with all its colorful inhabitants. For helping me through the last years of university.

My whole family, for all their help and support. Though most of them are still wondering what I am really doing in the lab :). My nephews, who allow me to be a child again and show me a world beyond physics.



# Bibliography

- [ABGP08] Alexia Auffèves, Benjamin Besga, Jean Michel Gérard, and Jean Philippe Poizat. Spontaneous emission spectrum of a two-level atom in a very-high-Q cavity. *Phys. Rev. A - At. Mol. Opt. Phys.*, 77(6):1–9, 2008.
- [AKN<sup>+</sup>11] R. Amsüss, Ch. Koller, T. Nöbauer, S. Putz, S. Rotter, K. Sandner, S. Schneider, M. Schramböck, G. Steinhauser, H. Ritsch, J. Schmiedmayer, and J. Majer. Cavity QED with Magnetically Coupled Collective Spin States. *Phys. Rev. Lett.*, 107(6):060502, August 2011.
- [Ams13] Robert Amsuess. Strong coupling of an NV spin ensemble to a superconducting resonator. 2013.
- [BGW<sup>+</sup>07] Alexandre Blais, Jay Gambetta, A. Wallraff, D. I. Schuster, S. M. Girvin, M. H. Devoret, and R. J. Schoelkopf. Quantum-information processing with circuit quantum electrodynamics. *Phys. Rev. A - At. Mol. Opt. Phys.*, 75(3):1–21, 2007.
- [BHW<sup>+</sup>04] Alexandre Blais, Ren Shou Huang, Andreas Wallraff, S. M. Girvin, and R. J. Schoelkopf. Cavity quantum electrodynamics for superconducting electrical circuits: An architecture for quantum computation. *Phys. Rev. A - At. Mol. Opt. Phys.*, 69(6):062320–1, 2004.
- [BNT<sup>+</sup>09] Gopalakrishnan Balasubramanian, Philipp Neumann, Daniel Twitchen, Matthew Markham, Roman Kolesov, Norikazu Mizuochi, Junichi Isoya, Jocelyn Achard, Johannes Beck, Julia Tissler, Vincent Jacques, Philip R Hemmer, Fedor Jelezko, and Jörg Wrachtrup. Ultralong spin coherence time in isotopically engineered diamond. *Nat. Mater.*, 8(5):383–387, 2009.
- [CC97] Erli Chen and SY Chou. Characteristics of coplanar transmission lines on multilayer substrates: Modeling and experiments. *IEEE Trans. Microw. theory . . .*, 45(6):939–945, 1997.

- [CG84] M. J. Collett and C. W. Gardiner. Squeezing of intracavity and traveling-wave light fields produced in parametric amplification. *Phys. Rev. A*, 30(3):1386–1391, 1984.
- [Dic54] RH Dicke. Coherence in spontaneous radiation processes. *Phys. Rev.*, 24(1), 1954.
- [Dru81] P. Drummond. Optical bistability in a radially varying mode. *IEEE J. Quantum Electron.*, 17(3):301–306, 1981.
- [DWM04] M. H. Mh Devoret, a Wallraff, and Jm M. Martinis. Superconducting Qubits: A Short Review. *Arxiv Prepr. cond-mat/0411174*, page 41, 2004.
- [Dys49] FJ Dyson. The S matrix in quantum electrodynamics. *Phys. Rev.*, 75(11), 1949.
- [E.81] Warburg E. Magnetische Untersuchungen über einige Wirkungen der Koerzitivkraft. *Ann. Phys. (N. Y.)*, 13:141–164, 1881.
- [FBB<sup>+</sup>09] J. M. Fink, R. Bianchetti, M. Baur, M. Göppl, L. Steffen, S. Filipp, P. J. Leek, a. Blais, and a. Wallraff. Dressed collective qubit states and the Tavis-Cummings model in circuit QED. *Phys. Rev. Lett.*, 103(8):1–4, 2009.
- [FEN<sup>+</sup>09] S. Felton, a. M. Edmonds, M. E. Newton, P. M. Martineau, D. Fisher, D. J. Twitchen, and J. M. Baker. Hyperfine interaction in the ground state of the negatively charged nitrogen vacancy center in diamond. *Phys. Rev. B - Condens. Matter Mater. Phys.*, 79(7):1–8, 2009.
- [FGF<sup>+</sup>08] A Fragner, M Göppl, J M Fink, M Baur, R Bianchetti, P J Leek, A Blais, and A Wallraff. Resolving vacuum fluctuations in an electrical circuit by measuring the Lamb shift. *Science*, 322(5906):1357–1360, 2008.
- [FGF<sup>+</sup>11a] S. Filipp, M. Göppl, J. M. Fink, M. Baur, R. Bianchetti, L. Steffen, and a. Wallraff. Multimode mediated qubit-qubit coupling and dark-state symmetries in circuit quantum electrodynamics. *Phys. Rev. A - At. Mol. Opt. Phys.*, 83(6):1–9, 2011.
- [FGF<sup>+</sup>11b] S. Filipp, M. Göppl, J. M. Fink, M. Baur, R. Bianchetti, L. Steffen, and a. Wallraff. Multimode mediated qubit-qubit coupling and dark-state symmetries in circuit quantum electrodynamics. *Phys. Rev. A - At. Mol. Opt. Phys.*, 83(6):1–9, 2011.
- [Fox10] Mike Fox. Quantum Optics: An Introduction. *Himal. Phys.*, 2010.



- [FWS<sup>+</sup>05] L. Frunzio, a. Wallraff, D. Schuster, J. Majer, and R. Schoelkopf. Fabrication and Characterization of Superconducting Circuit QED Devices for Quantum Computation. *IEEE Trans. Appiled Supercond.*, 15(2):860–863, June 2005.
- [Gar10] Damien Garcia. Robust smoothing of gridded data in one and higher dimensions with missing values. *Comput. Stat. Data Anal.*, 54(4):1167–1178, April 2010.
- [Gar11] Barry M Garraway. The Dicke model in quantum optics: Dicke model revisited. *Philos. Trans. A. Math. Phys. Eng. Sci.*, 369(1939):1137–55, March 2011.
- [Gha09] Ajoy Ghatak. *Optics*. McGraw Hill Higher Education, 2009.
- [HGHR98] Gerald Hechenblaikner, Markus Gangl, Peter Horak, and Helmut Ritsch. Cooling an atom in a weakly driven high-Q cavity. *Phys. Rev. A*, 58(4):3030–3042, October 1998.
- [HP40] T. Holstein and H. Primakoff. Field dependence of the intrinsic domain magnetization of a ferromagnet. *Phys. Rev.*, 58(12):1098–1113, 1940.
- [HRP<sup>+</sup>06] T Hime, P A Reichardt, B L T Plourde, T L Robertson, C-E Wu, A V Ustinov, and John Clarke. Solid-state qubits with current-controlled coupling. *Science*, 314(5804):1427–1429, 2006.
- [HSM06] J. Harrison, M. J. Sellars, and N. B. Manson. Measurement of the optically induced spin polarisation of N-V centres in diamond. *Diam. Relat. Mater.*, 15(4-8):586–588, 2006.
- [Ima09] Atac Imamoglu. Cavity QED Based on Collective Magnetic Dipole Coupling: Spin Ensembles as Hybrid Two-Level Systems. *Phys. Rev. Lett.*, 102(8):083602, February 2009.
- [JBZ<sup>+</sup>05] D. C. Johnston, S. H. Baek, X. Zong, F. Borsa, J. Schmalian, and S. Kondo. Dynamics of magnetic defects in heavy fermion LiV2O4 from stretched exponential Li7 NMR relaxation. *Phys. Rev. Lett.*, 95(17):5–8, 2005.
- [JC63] E.T. Jaynes and F.W. Cummings. Comparison of quantum and semiclassical radiation theories with application to the beam maser. *Proc. IEEE*, 51(1), 1963.
- [Joh06] D. C. Johnston. Stretched exponential relaxation arising from a continuous sum of exponential decays. *Phys. Rev. B - Condens. Matter Mater. Phys.*, 74(18):1–7, 2006.

- [JW06] F. Jelezko and J. Wrachtrup. Single defect centres in diamond: A review. *Phys. Status Solidi*, 203(13):3207–3225, October 2006.
- [Kat04] Ogata Katsuhiko. *System Dynamics*. 2004.
- [KGG<sup>+</sup>83] Y. Kaluzny, P. Goy, M. Gross, J. M. Raimond, and S. Haroche. Observation of self-induced Rabi oscillations in two-level atoms excited inside a resonant cavity: The ringing regime of superradiance. *Phys. Rev. Lett.*, 51(13):1175–1178, 1983.
- [KM91] Abraham Klein and E. R. Marshalek. Boson realizations of Lie algebras with applications to nuclear physics. *Rev. Mod. Phys.*, 63(2):375–558, 1991.
- [KOB<sup>+</sup>10] Y. Kubo, F. R. Ong, P. Bertet, D. Vion, V. Jacques, D. Zheng, a. Dréau, J.-F. Roch, a. Auffeves, F. Jelezko, J. Wrachtrup, M. F. Barthe, P. Bergonzo, and D. Esteve. Strong Coupling of a Spin Ensemble to a Superconducting Resonator. *Phys. Rev. Lett.*, 105(14):140502, September 2010.
- [Kol12] Christian Koller. Towards the experimental realization of Hybrid Quantum Systems. 2012.
- [KWM11] Z. Kurucz, J. H. Wesenberg, and K. Mølmer. Spectroscopic properties of inhomogeneously broadened spin ensembles in a cavity. *Phys. Rev. A*, 83(5):053852, May 2011.
- [Lax66] Melvin Lax. Classical noise IV: Langevin methods. *Rev. Mod. Phys.*, 38(3):541–566, 1966.
- [MCG<sup>+</sup>07] J Majer, J M Chow, J M Gambetta, Jens Koch, B R Johnson, J a Schreier, L Frunzio, D I Schuster, a a Houck, a Wallraff, a Blais, M H Devoret, S M Girvin, and R J Schoelkopf. Coupling superconducting qubits via a cavity bus. *Nature*, 449(7161):443–7, September 2007.
- [Ors07] Miguel Orszag. *Quantum Optics*. 2007.
- [PGPT01] V. Pecharsky, K. Gschneidner, A. Pecharsky, and A. Tishin. Thermodynamics of the magnetocaloric effect, 2001.
- [Phi99] J C Phillips. Stretched exponential relaxation in molecular and electronic glasses. *Reports Prog. Phys.*, 59(9):1133–1207, 1999.
- [PKA<sup>+</sup>14] Stefan Putz, Dmitry O Krimer, Robert. Amsüss, Abhilash Valookaran, Tobias Nöbauer, Jörg Schmiedmayer, Stefan Rotter, and Johannes Majer. Protecting a Spin Ensemble against Decoherence in the Strong-Coupling Regime of Cavity QED. *arXiv*, 10(October):1404.4169, 2014.

- [Poz11] M. David Pozar. *Microwave Engineering*. John Wiley & Sons, 4th edition, 2011.
- [QQ03] Entangled Macroscopic Quantum and Superconducting Qubits. Entangled Macroscopic Quantum. *Science (80-. )*, 300(June):1548–1550, 2003.
- [RDD<sup>+</sup>06] P. Rabl, D. Demille, J. M. Doyle, M. D. Lukin, R. J. Schoelkopf, and P. Zoller. Hybrid quantum processors: Molecular ensembles as quantum memory for solid state circuits. *Phys. Rev. Lett.*, 97(3):1–4, 2006.
- [RFDR13] J. Romero Gómez, R. Ferreiro Garcia, a. De Miguel Catoira, and M. Romero Gómez. Magnetocaloric effect: A review of the thermodynamic cycles in magnetic refrigeration. *Renew. Sustain. Energy Rev.*, 17:74–82, January 2013.
- [RTB<sup>+</sup>89] M. G. Raizen, R. J. Thompson, R. J. Brecha, H. J. Kimble, and H. J. Carmichael. Normal-mode splitting and linewidth averaging for two-state atoms in an optical cavity. *Phys. Rev. Lett.*, 63(3):240–243, 1989.
- [SCG11] Benjamin Smeltzer, Lilian Childress, and Adam Gali. <sup>13</sup>C Hyperfine interactions in the nitrogen-vacancy centre in diamond. *New J. Phys.*, 13, 2011.
- [SCLD14] Romana Schirhagl, Kevin Chang, Michael Loretz, and Christian L Degen. Nitrogen-vacancy centers in diamond: nanoscale sensors for physics and biology. *Annu. Rev. Phys. Chem.*, 65:83–105, 2014.
- [Sim01] RN Simons. *Coplanar waveguide circuits, components, and systems*. 2001.
- [SRA<sup>+</sup>12] K. Sandner, H. Ritsch, R. Amsüss, Ch. Koller, T. Nöbauer, S. Putz, J. Schmiedmayer, and J. Majer. Strong magnetic coupling of an inhomogeneous nitrogen-vacancy ensemble to a cavity. *Phys. Rev. A*, 85(5):053806, May 2012.
- [SZA<sup>+</sup>13] Shiro Saito, Xiaobo Zhu, Robert Amsüss, Yuichiro Matsuzaki, Kosuke Kakyuanagi, Takaaki Shimo-Oka, Norikazu Mizuochi, Kae Nemoto, William J. Munro, and Kouichi Semba. Towards realizing a quantum memory for a superconducting qubit: Storage and retrieval of quantum states. *Phys. Rev. Lett.*, 111(10):1–5, 2013.
- [TC68] Michael Tavis and FW Cummings. Exact solution for an N-molecule—radiation-field Hamiltonian. *Phys. Rev.*, 170(2), 1968.

- [TCC<sup>+</sup>08] J. M. Taylor, P. Cappellaro, L. Childress, L. Jiang, D. Budker, P. R. Hemmer, a. Yacoby, R. Walsworth, and M. D. Lukin. High-sensitivity diamond magnetometer with nanoscale resolution. 4(October):29, 2008.
- [TS03] AM Tishin and YI Spichkin. *The Magnetocaloric Effect and Its Applications*. 2003.
- [VZK<sup>+</sup>09] J. Verdú, H. Zoubi, Ch. Koller, J. Majer, H. Ritsch, and J. Schmiedmayer. Strong Magnetic Coupling of an Ultracold Gas to a Superconducting Waveguide Cavity. *Phys. Rev. Lett.*, 103(4):043603, July 2009.
- [WAB<sup>+</sup>09] J. H. Wesenberg, a. Ardavan, G. a D Briggs, J. J L Morton, R. J. Schoelkopf, D. I. Schuster, and K. Mølmer. Quantum computing with an electron spin ensemble. *Phys. Rev. Lett.*, 103(7):1–4, 2009.
- [WJ06] Jörg Wrachtrup and Fedor Jelezko. Processing quantum information in diamond. *J. Phys. Condens. Matter*, 18(21):S807–S824, 2006.
- [wPa] AZ www.pcmojo.com PC Mojo - Cave Creek. Coplanar Waveguide- Microwave Encyclopedia - Microwaves101.com.
- [wPb] AZ www.pcmojo.com PC Mojo - Cave Creek. Transverse Electro-Magnetic - Microwave Encyclopedia - Microwaves101.com.
- [WRHK99] J a Van Wyk, E C Reynhardt, G L High, and I Kiflawi. The dependences of ESR line widths and spin - spin relaxation times of single nitrogen defects on the concentration of nitrogen defects in diamond. *J. Phys. D. Appl. Phys.*, 30(12):1790–1793, 1999.
- [XAYN13] ZL Xiang, Sahel Ashhab, JQ You, and Franco Nori. Hybrid quantum circuits: Superconducting circuits interacting with other quantum systems. *Rev. Mod. Phys.*, 2013.
- [YPA<sup>+</sup>06] T. Yamamoto, Yu a. Pashkin, O. Astafiev, Y. Nakamura, and J. S. Tsai. Conditional gate operation in superconducting charge qubits. *Quantum Comput. Solid State Syst.*, (i):10–18, 2006.